Icarus 264 (2016) 369–386

Contents lists available at ScienceDirect

Icarus

journal homepage: www.journals.elsevier.com/icarus

An improved model for interplanetary dust fluxes in the outer Solar System

Andrew R. Poppe

Space Sciences Laboratory, 7 Gauss Way, University of California at Berkeley, Berkeley, CA 94720, USA

ARTICLE INFO

Article history:
Received 15 April 2015
Revised 31 July 2015
Accepted 3 October 2015
Available online 14 October 2015

Keywords:
Interplanetary dust
Debris disks
Kuiper belt
Atmospheres, composition
Photochemistry

ABSTRACT

We present an improved model for interplanetary dust grain fluxes in the outer Solar System constrained by in situ dust density observations. A dynamical dust grain tracing code is used to establish relative dust grain densities and three-dimensional velocity distributions in the outer Solar System for four main sources of dust grains: Jupiter-family comets, Halley-type comets, Oort-Cloud comets, and Edgeworth-Kuiper Belt objects. Model densities are constrained by in situ dust measurements by the *New Horizons* Student Dust Counter, the *Pioneer* 10 meteoroid detector, and the *Galileo* Dust Detection System (DDS). The model predicts that Jupiter-family comet grains dominate the interplanetary dust grain mass flux inside approximately 10 AU, Oort-Cloud cometary grains may dominate between 10 and 25 AU, and Edgeworth-Kuiper Belt grains are dominant outside 25 AU. The model also predicts that while the total interplanetary mass flux at Jupiter roughly matches that inferred by the analysis of the *Galileo* DDS measurements, mass fluxes to Saturn, Uranus, and Neptune are at least one order-of-magnitude lower than that predicted by extrapolations of dust grain flux models from 1 AU. Finally, we compare the model predictions of interplanetary dust oxygen influx to the giant planet atmospheres with various observational and photochemical constraints and generally find good agreement, with the exception of Jupiter, which suggests the possibility of additional chemical pathways for exogenous oxygen in Jupiter's atmosphere.

1. Introduction

Interplanetary dust grains pervade the Solar System and are an important driver of several physical processes. These include, for example, the production of tenuous rings and dusty exospheres around planetary satellites (e.g., Thiessenhusen et al., 2002; Verbiscer et al., 2009; Hedman et al., 2009; Poppe and Horányi, 2011), the spatial and compositional evolution of Saturn's main planetary ring system (Durisen et al., 1989; Cuzzi and Estrada, 1998; Estrada et al., 2015), the possible injection of meteoric metal ions into the magnetospheres of the giant planets (Christon et al., 2015), and the alteration of neutral chemistry and ion densities in the atmospheres of the giant planets and Titan through meteoric ablation (e.g., Moses, 1992; Feuchtgruber et al., 1997, 1999; Moses et al., 2000; Moses and Bass, 2000; Molina-Cuberos et al., 2001). The interplanetary dust grain environment in the inner Solar System has been the subject of extensive modeling (e.g., Grün et al., 1985; Divine, 1993; Kortenkamp and Dermott, 1998; Dikarev et al., 2005; Nesvorný et al., 2010), in situ flux measurements (Dietzel et al., 1973; Love and Brownlee, 1993; Hillier et al., 2007; St. Cyr et al., 2009; Poppe et al., 2011), and remote sensing observations (Leinert, 1975; Hauser et al., 1984; Hahn et al., 2002; Janches and ReVelle, 2005; Janches et al., 2006). Additionally, it has been recently shown from a comparison of dynamical modeling and observations by the *Infrared Astronomical Satellite* (IRAS) that for the inner Solar System, interplanetary dust is mainly supplied by Jupiter-family comets, with small additional contributions from asteroids and Oort-Cloud comets (Nesvorný et al., 2010).

The picture for the outer Solar System, however, is not as clear. Extending from approximately 35 to 50 AU, the Edgeworth-Kuiper Belt (EKB) is thought to be the main source of interplanetary dust grains in the outer Solar System, with some cometary contribution(s) as well (Landgraf et al., 2002). EKB grains, produced through either mutual EKB object collisions and interstellar/interplanetary dust bombardment (Stern, 1996; Yamamoto and Mukai, 1998; Poppe, 2015), diffuse throughout the EKB region and the outer Solar System as they are subjected to a variety of forces, including, but not limited to, solar and planetary gravitation, solar wind and Poynting–Robertson drag, and stellar radiation pressure (Burns et al., 1979; Gustafson, 1994; Horányi, 1996). As dust grains spiral in from the EKB region under the influence of Poynting–Robertson

E-mail address: poppe@ssl.berkeley.edu

http://dx.doi.org/10.1016/j.icarus.2015.10.001
0019-1035/

drag, their motion is often dominated by resonant gravitational interactions with Neptune, which serve to trap grains in mean-motion resonances (MMRs) outside of 30 AU (Liou and Zook, 1997, 1999; Moro-Martín and Malhotra, 2002, 2003), a phenomenon which may be observable in observations of other nascent exozodical disks (e.g., Greaves et al., 1998; Wyatt et al., 1999; Lisse et al., 2007a, 2008, 2009, 2012; Stark and Kuchner, 2008; Moro-Martín et al., 2010). Eventually, the grains break free of these resonances to continue their progression inwards past the outer planets, before either being ejected from the Solar System by one of the planets (usually Jupiter or Saturn) or making their way into the inner Solar System. More recent dynamical models have begun to explore the role that grain–grain collisions have on the equilibrium density, especially in the Edgeworth-Kuiper Belt where Poynting–Robertson decay times are equal to or significantly longer than expected collisional destruction times (Stark and Kuchner, 2009; Kuchner and Stark, 2010; Vitense et al., 2014). Some recent dynamical dust models have used either in situ dust density measurements (i.e., *Pioneer* 10/11 meteoroid detectors and the *New Horizons* Student Dust Counter) or remote sensing observations of zodiacal brightness to constrain the production rates of various interplanetary dust grain sources (Nesvorný et al., 2010; Han et al., 2011).

In light of the fundamental importance of interplanetary dust grain fluxes on various planetary processes in the outer Solar System, the recent developments in the understanding of how grain–grain collisions affect dust grain densities, the availability of both in situ and remote sensing constraints on various sub-populations of the interplanetary dust, and the long-persisting overall uncertainty of outer Solar System dust fluxes, we are motivated to develop a comprehensive model of the interplanetary dust grain environment in the outer Solar System. The model presented here combines the main interplanetary dust grain sources, relevant physics for both dust grain dynamical evolution and collisions, and several in situ constraints on dust densities. Section 2 describes the model, including the parent source bodies and the dynamical evolution of the dust, Section 3 describes the model results and the constraints imposed by available measurements, Section 4 compares the influx of oxygen from interplanetary dust grains to the atmospheres of the outer planets with observational constraints, and Section 5 discusses the results and presents conclusions.

2. Model description

The dust dynamics model is built on that used previously in Han et al. (2011), Poppe and Horányi (2012), and Poppe (2015) with several important enhancements. These include more accurate, observationally-constrained EKB object (EKBO) parent body populations (Petit et al., 2011), modeling of cometary dust grain sources, and the inclusion of a collisional algorithm for Edgeworth-Kuiper Belt dust grains (Stark and Kuchner, 2009; Kuchner and Stark, 2010). Individual dust grains are launched from a collection of parent bodies (see Section 2.1 and Appendix A) and their trajectories are traced using a Bulirsch–Stoer step-size controlled integrator (Press et al., 2007). The equation of motion for an individual dust grain is given by,

$$\ddot{\mathbf{r}}_s = -\frac{GM_\odot}{r_s^3}\mathbf{r_s} - \sum_{i=1}^{4}\frac{GM_i}{r_i^3}\mathbf{r_i} + \frac{1}{m}\mathbf{F_L} + \frac{\pi a_d^2}{mc}SQ_{pr}\left[\left(1-(1+w)\frac{\dot{r}_s}{c}\right)\hat{\mathbf{r}}_\mathbf{s} - (1+w)\frac{\dot{\mathbf{r}}_\mathbf{s}}{c}\right], \quad (1)$$

where $\mathbf{r_j}$, $\dot{\mathbf{r}}_\mathbf{j}$, and $\ddot{\mathbf{r}}_\mathbf{j}$ are the position, velocity, and acceleration vectors of the dust grain with respect to the Sun ($j = s$) or the outer planets, Jupiter to Neptune, ($j = i$), $M_\odot$ and M_i are the masses of the Sun and the planets, respectively, $\mathbf{F_L}$ is the Lorentz force, S is the radiation flux density, $Q_{pr} = 1$ is the radiation pressure coefficient (typically valid for $a \gtrsim 0.5$ μm), and $w = 0.35$ is a constant ratio between solar wind drag and Poynting–Robertson drag (Burns et al., 1979; Gustafson, 1994; Liou et al., 1995). The Lorentz force is $\mathbf{F_L} = q(\dot{\mathbf{r}}_\mathbf{s} \times \mathbf{B})$, where q is the grain charge and $\mathbf{B}$ is the interplanetary magnetic field. We use the interplanetary magnetic field model described by Landgraf et al. (2000) and assume a constant electrostatic potential on all grains, $\phi = +5$ V, yielding a size-dependent grain charge, $q = 4\pi\epsilon_o a_d \phi$ (Horányi, 1996). Modeled grain sizes span from 10^{-12} g to 10^{-5} g in half-logarithmic intervals (i.e., $[10^{-12}, 10^{-11.5}, 10^{-11}, \ldots, 10^{-5.5}, 10^{-5}]$ g), which assuming a density of $\rho = 2.5$ g cm^{-3} spans sizes from approximately 0.5 μm to 100 μm. In terms of the ratio of the radiation pressure force to the solar gravitational force, β, the particles range from 0.46 to 0.0023.

2.1. Dust grain sources

The model includes four separate dust grain source populations: Edgeworth-Kuiper Belt objects (EKBOs), Jupiter-family comets (i.e., Levison and Duncan, 1997), Halley-type comets, and Oort-Cloud comets (Oort, 1950; Francis, 2005). Each of these populations contributes dust to the interplanetary medium either through active outgassing or disruptive outbursts in the case of comets or from either mutual collisions (Stern, 1996) and interstellar or interplanetary dust grain bombardment in the case of EKBOs (Yamamoto and Mukai, 1998; Poppe, 2015). An accurate description of the parent body orbital distributions is essential to modeling dust grain equilibria in the Solar System, as dust grains ejected with different initial conditions can yield significantly different spatial and velocity distributions. Table 1 summarizes the main orbital characteristics of each of the dust grain sources, with a full description provided in Appendix A.

Similar to previous models, we must ensure that enough grains are simulated to prevent the spurious dominance of individual grains with relatively long lifetimes due to trapping in MMRs when calculating equilibrium density and velocity distributions (Moro-Martín and Malhotra, 2002). For EKB grains, which are particularly susceptible to capture in MMRs and therefore have longer lifetimes, we ran approximately 2500 grains for each size bin, yielding roughly 37,500 EKB grains in total. For JFC and HTC grains, with relatively shorter dynamical lifetimes, we ran 6000 grains per size bin for each type, for a total of nearly 100,000 grains for both types. For OCC grains, we ran 1200 grains per size, except for the largest three grain sizes (10^{-6}, $10^{-6.5}$, and 10^{-5} g, or equivalently 50, 70, and 100 μm), where we doubled the number of grains (2400 per size bin). The additional grains for these largest sizes were deemed necessary based on inspection of equilibrium densities with only 1200 grains, which suffered from somewhat poor statistics. For all

Table 1
A description of the various dust grain sources used in the model. See Appendix A for a full discussion.

Type	Description
Edgeworth-Kuiper Belt	See Table A.3
Jupiter-family comets	$f(a,e)$ from Levison and Duncan (1997) $dN(i) \propto \sin(i)\exp^{-0.5(i/\sigma_J)^2}$
Halley-type comets	$20 < P < 200$ years, $(7.5 < a < 34$ AU) $0.9 < e < 0.99$ $dN(i) \propto \sin(i)\exp^{-0.5(i/\sigma_H)^2}$
Oort Cloud comets	$1000 < a < 10,000$ AU $dN(q) = \{1+\sqrt{q},\ q < 2$ AU; $2.41(q/2)^7,\ q > 2$ AU$\}$ $dN(i) \propto \sin(i)$

cometary sources (JFC, HTC, and OCC grains), we did not apply a weighting for the dependence of cometary dust grain emission and outburst activity as a function of distance from perihelion. This choice is motivated by the observations of cometary activity at distances greater than individual comet perihelia (e.g., Fulle, 1992; Sekanina, 1996; Kelley et al., 2013).

2.2. Collisional algorithm for EKB grains

An important improvement of our model here over previous versions is the inclusion of a collisional grinding algorithm for EKB grains, adopted from that described by Stark and Kuchner (2009) and Kuchner and Stark (2010). The necessity of the collisional algorithm is driven by both the relatively long Poynting–Robertson lifetimes of EKB grains and the extended lifetimes of EKB grains due to trapping in MMRs with respect to their mutual collisional lifetimes, especially for larger sized grains. At this time, we only apply the collisional model to the EKB grains and not other sources. Our implementation closely follows that of Stark and Kuchner (2009), who showed via extensive testing and comparison to analytic expressions (where available) that the algorithm produces both a unique and correct solution for collisional effects on a debris disk (given certain conditions on the algorithm with respect to sufficient grain statistics and bin sizes, for example).

First, we run a "seed" model of all EKB dust grains with no mutual collisions. We then re-trace each dust grain through the seed model, calculating the collisional depth, $\tau_{c,i}$, for each particle at time-step i as (adapted from Eq. (4), Stark and Kuchner, 2009),

$$\tau_{c,i} \approx \sum_k n_k \sigma_k |\mathbf{v_i} - \mathbf{v_k}| t_i, \tag{2}$$

where n_k, σ_k, and $\mathbf{v_k}$ are the local density, cross-section, and velocity of the kth particle in the local bin and t_i is the time step of the grain model. The k index sums over all sizes and types of EKB grains, from 0.5 μm to 100 μm at the location of the grain at time i. Using the collisional depth for each grain as a function of time along its trajectory, we then calculate the weight of the grain, w_i, as,

$$w_i = w_{i-1} e^{-\tau_{c,i}}. \tag{3}$$

Thus, as time progresses along the dust grain trajectory, the weight of the particle is decreased according to its probability of having been destroyed in a mutual collision. Using these newly-calculated weights, we then re-calculate the dust grain densities and velocity distributions and repeat the re-tracing of all grains. Following Stark and Kuchner (2009), this process is iterated several times (typically 5–6) before the model results come to an equilibrium with minimal change (<5%) from one iteration to the next. Currently, our model does not generate secondary collisional debris from grain–grain collisions. Collisional fragmentation and production of secondary debris may be an important factor in the overall density distributions of grains, especially for smaller grains (which have sources not only from the parent bodies but from fragmentation of larger grain sizes); however, as discussed by Kuchner and Stark (2010), cometary dust grains are often loosely-bound aggregates of smaller grains (A'Hearn et al., 2005; Brownlee et al., 2006), which can easily be expelled from the Solar System via radiation pressure after collisional disruption (i.e., so-called β-meteoroids). Additionally, we have not included sizes larger than 100 μm in either the dynamical modeling or the collisional grinding algorithm for EKB grains due to computational constraints. The absence of the >100 μm grain population may affect the equilibrium distribution of EKB grains somewhat, but at this time, we feel that most of the effect of collisions on the EKB grains has been captured using 0.5–100 μm grains. Future versions of the model, with increased computational resources, should be able to capture grains up to 1 mm in the EKB.

Fig. 1 shows an example of the collisional algorithm for 30 μm cold EKB grains. Panel (a), in upper left, shows the seed model of 30 μm cold EKB grains before any collisions are applied. Similar to previous work (Liou and Zook, 1999; Moro-Martín and Malhotra, 2002, 2003), strong indications of mean-motion resonances (MMRs) are seen in the equilibrium density distribution such as sharp structures and edges. The 30 μm cold density is mainly concentrated from 30 to 55 AU, drops off steeply inside the orbit of Neptune (dashed line), remains at a fairly constant level between Neptune and the orbit of Jupiter, before decreasing again inside 5 AU. Panel (b) shows the 30 μm cold equilibrium density after the first iteration of the collisional algorithm as described above. The value printed above the plot (≈0.17 for panel (b)) denotes the total fraction of grains relative to the seed model left in the simulation after collisions have been applied. Thus, for this initial step, nearly 83% of the 30 μm cold grains have been collisionally destroyed. As noted by Stark and Kuchner (2009), this first iteration over-estimates the amount of collisions, and thus, the algorithm is iteratively applied, using the previous density as input. Such iteration is seen in panels (b) through (f), with the net remaining density of 30 μm cold EKB grains quickly converging to ≈23% of the original density. Collisions have erased nearly all of the detailed signatures of MMRs, with only slight asymmetries in the density at both the location of Neptune and 180° from Neptune. The 30 μm cold densities still decline sharply in density inside the orbit of Neptune, similar to the non-collisional case (panel (a)). Thus, we are able to reproduce the results of Stark and Kuchner (2009) and Kuchner and Stark (2010) in finding that mutual collisional destruction of EKB dust grains can heavily influence the equilibrium density distributions. We apply the collisional algorithm to all EKB sizes and sub-types (cold, hot, resonant, outer) for all results presented below.

3. Model results

3.1. Equilibrium densities

Fig. 2 shows the equilibrium column densities in the ecliptic plane for 1, 5, 20, and 100 μm grains from the Edgeworth-Kuiper Belt (EKB), Jupiter-family comets (JFC), Halley-type comets (HTC), and Oort-Cloud comets (OCC), respectively. Each panel is individually normalized to its own maximum for comparison. The EKB dust grain densities, shown in the left-most column, exhibit a strong dependence on grain size, with smaller grains forming a much more diffuse cloud throughout the outer and inner Solar System, while larger grains (starting with ≈5 μm) showing successively more trapping outside the orbit of Neptune and less density inside the orbit of Neptune. For the largest size modeled here, 100 μm, less than one grain in 1000 is successfully able to reach the inner Solar System. JFC grains, shown in the second column, exhibit little variation as a function of size. JFC grain densities peak in the inner Solar System and extend out to the orbit of Neptune at levels of only $\approx 10^{-4}$. Close inspection reveals evidence of JFC grain trapping in an MMR just outside the orbit of Jupiter, stronger for larger JFC grains. HTC grains, in the third column, are also concentrated in the inner Solar System, yet extend farther out past of the orbit of Neptune, reflecting the larger semi-major axis distribution of Halley-type comets versus Jupiter-family comets. Some variation is seen as a function of size, with larger grains tending to have higher densities farther out in the Solar System, due to the longer Poynting–Robertson decay time for larger grains. Finally, OCC grain densities, shown in the right-most column, show a strong dependence on grain size. Smaller OCC grains (≈1 μm) have their maximum density in the inner Solar System while extending well past the orbit of Neptune at levels of 10^{-2}–10^{-1}. As the OCC grain size

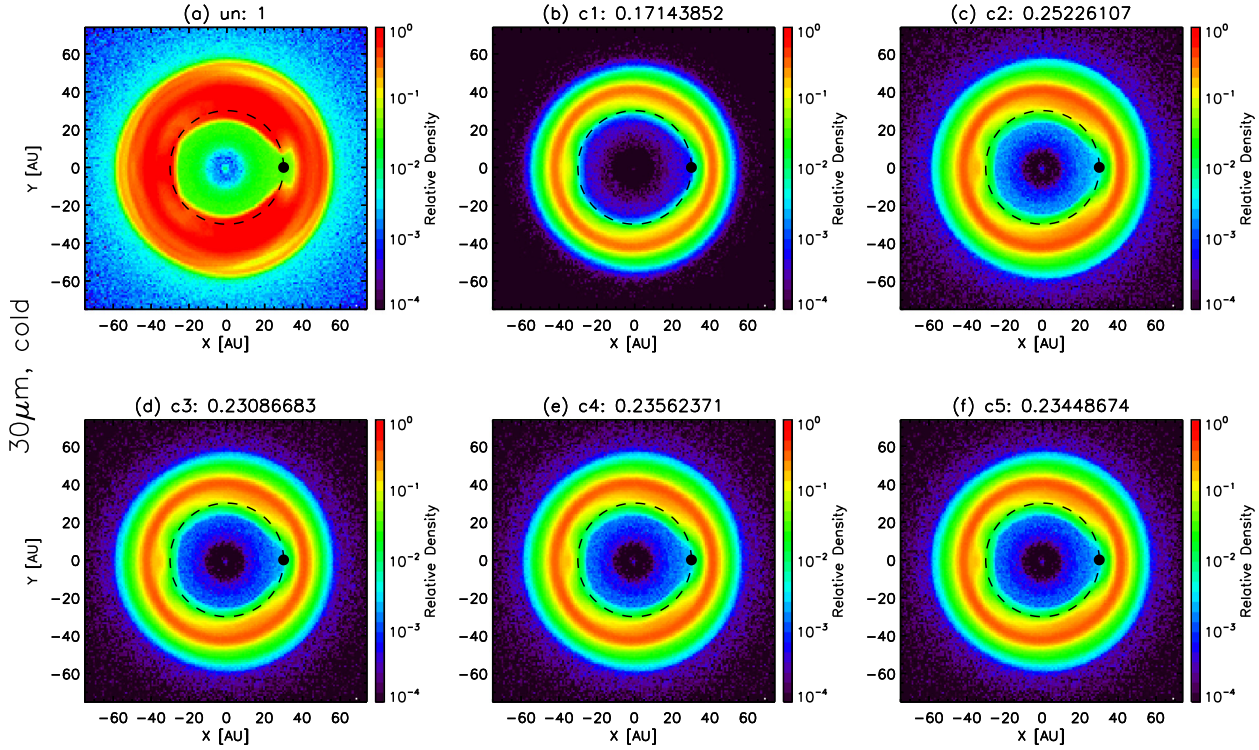

Fig. 1. Successive iterations of the collisional algorithm for 30 μm cold EKB grains (see Stark and Kuchner, 2009). The non-collisional, "seed" model is shown in upper left, with successive iterations shown left-to-right, row-by-row. The numerical value above each panel indicates the total fraction of grains present in the model after collisions are applied relative to the non-collisional case. Thus, for 30 μm cold grains, 23.4% of the grains remain after the algorithm is applied. The dashed line and dot show the orbit and location of Neptune, respectively.

increases, the Poynting-Robertson drift time increases and the grains are in turn more likely to be scattered by Jupiter and/or Saturn (the so-called "Jupiter-barrier") before entering the inner Solar System. Thus, the maximum density for 5 μm grains and larger progressively moves outward. For 100 μm, the density peaks approximately between the orbits of Uranus and Neptune and declines rapidly within 20 AU. Such a "rollover" in the OCC density distribution was noted previously by Nesvorný et al. (2011) who found that larger grains were significantly less able to penetrate into the inner Solar System and cross 1 AU.

3.2. Velocity distributions

In addition to calculating the net interplanetary mass flux to each of the outer planets, the model also provides three-dimensional velocity distributions for each species as a function of heliocentric distance. From the model, we select all grains that cross within 0.5 AU of the orbit of any of the outer planets and compute the relative impact speed at each planet's Hill radius before any local gravitational acceleration. Fig. 3 shows the 10 μm speed distributions for each dust grain family at each outer planet, where we have normalized each individual distribution so that $\int_0^\infty f(s)ds = 1$, where s is the impact speed, for comparison. At Jupiter, the velocity distributions for each species range from fairly slow JFC and EKB grains, with median impact speeds of 3.7 and 5.3 km/s, respectively, to HTC grains with a moderate median speed of 14 km/s, to OCC which have the fastest speed distribution with a median of 23 km/s. At Saturn, EKB grains are slowest with a median speed of 3.1 km/s, followed by JFC, HTC, and OCC grains at respective median impact speeds of 6.6, 11, and 16 km/s. All four species have much slower relative impact speeds at Uranus and Neptune given the greater heliocentric distance and slower Kepler velocities. EKB grains impact with a very low 1.0 km/s, JFC and HTC grains have approximately 4 km/s median impact speeds, while OCC tend to impact around 8.6 km/s. The mean speeds reported here are not perfect indicators as many of the distributions have extended tails or are non-Maxwellian. The OCC grain speed distributions show a subtle two-peaked distribution (for example, at Jupiter there is a main OCC speed peak at ≈ 26 km/s and a smaller secondary peak at 11 km/s). This is due to the presence of a dominant retrograde component and a smaller prograde component in the OCC population. The variations in impact velocity distributions both across species and at each outer planet implies a variable amount of gravitational focusing of the incoming IDP flux within each planetary system, discussed further in Section 3.6.

3.3. Constraints on the outer Solar System dust environment

3.3.1. In-situ constraints

In order to accurately construct a model of interplanetary dust fluxes in the outer Solar System, we must use all available constraints on the dust grain densities. Such information, however, is fairly limited, especially for the outer Solar System. Nevertheless, we briefly review the available constraints. In-situ interplanetary dust measurements have been made on several spacecraft in the inner Solar System (i.e., *Helios*, *Ulysses*, *Galileo*, *Cassini*, etc.) yet fewer in the outer Solar System. The *Voyager* 1 and 2 spacecraft reported observations of impact-produced plasma detected by the plasma wave instrument (Gurnett et al., 1997). Despite traveling significantly out of the ecliptic plane, the inferred dust density for $\approx 10^{-11}$ g grains remained essentially constant, implying that this population of grains originated most likely from cometary sources with a wide range of initial inclinations, as opposed to planetary and asteroidal sources that are mainly limited to the ecliptic plane. The *Pioneer* 10 and 11 spacecraft both carried meteoroid detectors that measured the impact flux of approximately 5

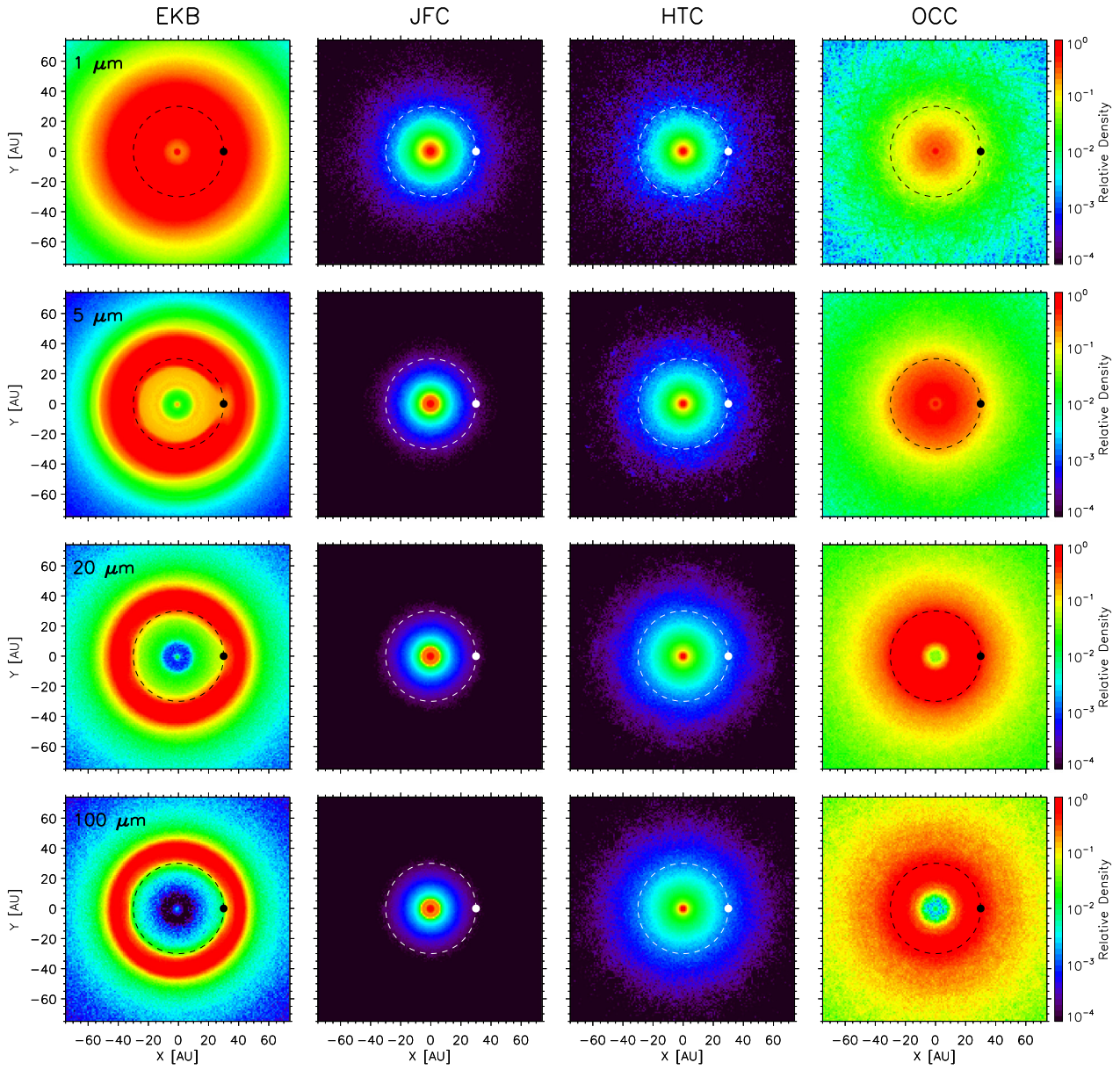

Fig. 2. The equilibrium density distributions for Edgeworth-Kuiper Belt (EKB), Jupiter-family comets (JFC), Halley-type comets (HTC), and Oort-Cloud comets (OCC) for 1, 5, 20, and 100 μm, all normalized to their respective maximum for comparison.

and 10 μm radius grains, respectively, as a function of heliocentric distance (Humes, 1980). *Pioneer* 11 made continuous measurements out to approximately 9 AU while *Pioneer* 10 reported measurements to nearly 18 AU. More recently, the *New Horizons* Student Dust (SDC) reported measurements of the cumulative flux of 0.5–5 μm dust grains from inside the orbit of Jupiter to almost 30 AU (Horányi et al., 2008; Poppe et al., 2010; Szalay et al., 2013).

Among these measurements, we use only the Student Dust Counter and Pioneer 10 results to constrain the model. For Pioneer 11, we considered the revised analysis of impact fluxes presented in Dikarev and Grün (2002), who attempted to account for the initial uncertainty in the number of active detection cells in the instrument; however, the interplanetary dust fluxes derived in Dikarev and Grün (2002) are *higher* than those of Pioneer 10 (Humes, 1980). Given that Pioneer 10 measured a smaller grain size than did Pioneer 11, this yields an inconsistency in that the equilibrium interplanetary dust grain size distribution should decrease with size, yet the combined results of Pioneer 10 from Humes (1980) and Pioneer 11 from Dikarev and Grün (2002) would imply a size distribution that *increases* with size. Such a result is clearly unphysical and thus, we do not include Pioneer 11 data in our analysis. Additionally, we do not use the Voyager 1/2 measurements due to significant uncertainty in the measured grain size.

At Jupiter, the *Galileo* Dust Detection System (DDS) made observations of several dust populations in the jovian system, including measurements of impact-induced ejecta clouds around three of the Galilean moons: Europa, Callisto, and Ganymede (Krüger et al., 1999, 2000, 2003). These ejecta clouds have then served as a means to estimate the total mass flux into the jovian system, through a series of data-model comparisons (Krivov et al., 2002; Sremčević et al., 2003, 2005). Krivov et al. (2002) estimated a total mass influx at Jupiter of approximately 7×10^{-13} g m^{-2} s^{-1} while a later analysis by Sremčević et al. (2005), which incorporated asymmetries in the incoming primary dust populations, suggested that the total mass flux to Jupiter estimate be revised slightly downward to

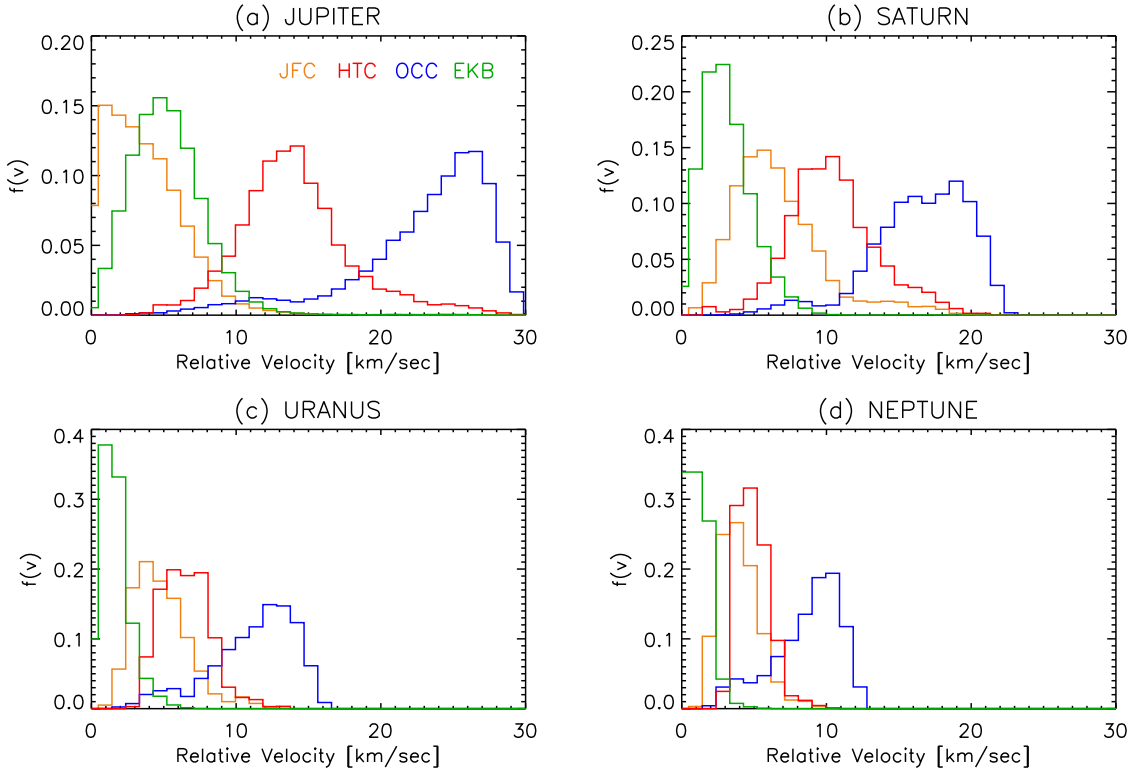

Fig. 3. The 10 μm velocity distribution for each family of dust grains at each of the giant planets, at the Hill radius before any local gravitational acceleration. Each individual distribution is normalized such that $\int_0^\infty f(s)ds = 1$, for comparison.

approximately 3×10^{-13} g m^{-2} s^{-1}. This estimate provides an important data point in calibrating the absolute flux and density of interplanetary dust grains in the outer Solar System and will be used to compare with our model.

3.3.2. Remote sensing constraints

One important constraint that drives some of the relative dust production rates in our model is the recent finding by Nesvorný et al. (2010) regarding the ultimate source of the interplanetary dust complex in the inner Solar System. Using a dynamical model and mid-infrared thermal emission observations from the IRAS satellite, Nesvorný et al. (2010) determined that Jupiter-family comets are the main source of interplanetary dust grains in the inner Solar System. Asteroidal and long-period comets were also found to contribute, although at relatively small levels (<10%). These results serve as an important overall consistency check on our model at 5 AU. While our model is not specifically suited for the inner Solar System in that it does not include asteroidal sources or gravitational forces from the inner terrestrial planets, our model, as described below, qualitatively matches that of Nesvorný et al. (2010) near Jupiter.

Finally, another method of determining upper limits to dust fluxes to each of the outer planets is available through the use of atmospheric compositional measurements. These constraints have come from a variety of observations including the *Infrared Space Observatory* (ISO), *Spitzer*, *Herschel*, and *Cassini* Composite Infrared Spectrometer (CIRS), for example (see Section 4). Early ISO observations reported the presence of external H_2O and CO_2 in the atmospheres of all the giant planets and Titan (Feuchtgruber et al., 1997, 1999) and attributed the presence of these molecules to the influx of external material, one source of which could be interplanetary dust (other sources include local ring particles and gases, satellite material, i.e., from the plumes of Saturn's moon Enceladus, quasi-steady delivery from small comets, or punctuated, bulk delivery from large cometary impacts). In addition to the well-known Shoemaker-Levy 9 impact at Jupiter, there exists evidence of large cometary impacts at the other giant planets (i.e., Lellouch et al., 2005; Hesman et al., 2007; Cavalié et al., 2010); thus, the total inferred molecular influx most likely cannot be solely attributed to that of interplanetary dust grain influx and ablation. Nevertheless, these observations do set upper limits to the net influx of exogenous oxygen. In Section 4, we compare our modeled influx of oxygen to each of the outer planet atmospheres with observational and photochemical modeling constraints.

3.4. Model constraints

Previous work has made progress towards identifying the major populations of dust grain sources in the Solar System and their relative levels of contribution. Nesvorný et al. (2010) have shown that JFC grains are the dominant contributor to the zodiacal cloud in the inner Solar System via comparison to IRAS observations, and thus, we expect that JFC grains will predominantly contribute at Jupiter. Landgraf et al. (2002) have suggested that for ≈5 μm grains, cometary grains dominate inside 7 AU while EKB grains are dominant outside of 7 AU. Theoretical analyses have provided estimates for the 0.1–10 μm production rate for the entire Edgeworth-Kuiper Belt for two different processes: (1) Stern (1996) provided an estimate of 8.6×10^4–2.9×10^7 g/s for dust grain production from mutual EKBO collisions and (2) Yamamoto and Mukai (1998) showed that similar levels, 3.7×10^5–3.1×10^7 g/s, could be provided by interstellar bombardment of EKB objects. A comparison of *New Horizons* SDC data to an earlier version of the dynamical dust model presented here yielded EKB production rates in line with both the Stern (1996) and Yamamoto and Mukai (1998) estimates of approximately 8.9×10^5 g/s for 0.1–10 μm grains (Han

et al., 2011), although we note that this version of the model did not include mutual EKB grain–grain collisions.

We focus first on the in situ measurements by the *New Horizons* Student Dust Counter (SDC) and the *Pioneer* 10 (P10) meteoroid detectors. Using the three-dimensional density and velocity distributions obtained from our dust model, we trace the trajectory of each spacecraft though the model for all dust species (EKB, JFC, HTC, and OCC) for all relevant sizes. For SDC, we include dust grains with radii, $0.5 < a < 5$ μm (Horányi et al., 2008), while for *Pioneer* 10, we select the cumulative flux of grains, $a > 5$ μm (Humes, 1980). For all grain families, we assume a production mass distribution of the form $dM/dm \propto m^{-\alpha/3}$, where $\alpha = 2.5$ (i.e., Borkowski and Dwek, 1995). Note that this is not the instantaneous mass distribution at any point in space after the grains have undergone migration from their parent bodies, but rather the initial distribution of grains produced from the objects themselves. We also quote all production rates as the 0.1–10 μm production rate in order to establish comparisons with previous theoretical work (Stern, 1996; Yamamoto and Mukai, 1998). Both instruments, SDC and P10, are assumed to point directly along the spacecraft velocity vector with instrument field-of-views (FOV) of 2π str. The velocity of the spacecraft is vector added to the dust grain velocity distribution at each point along the respective spacecraft trajectory and the resulting net flux computed. In order to determine the best fit to both the *Pioneer* 10 and SDC data, we compute χ^2 goodness-of-fit statistics for each spacecraft separately (Press et al., 2007).

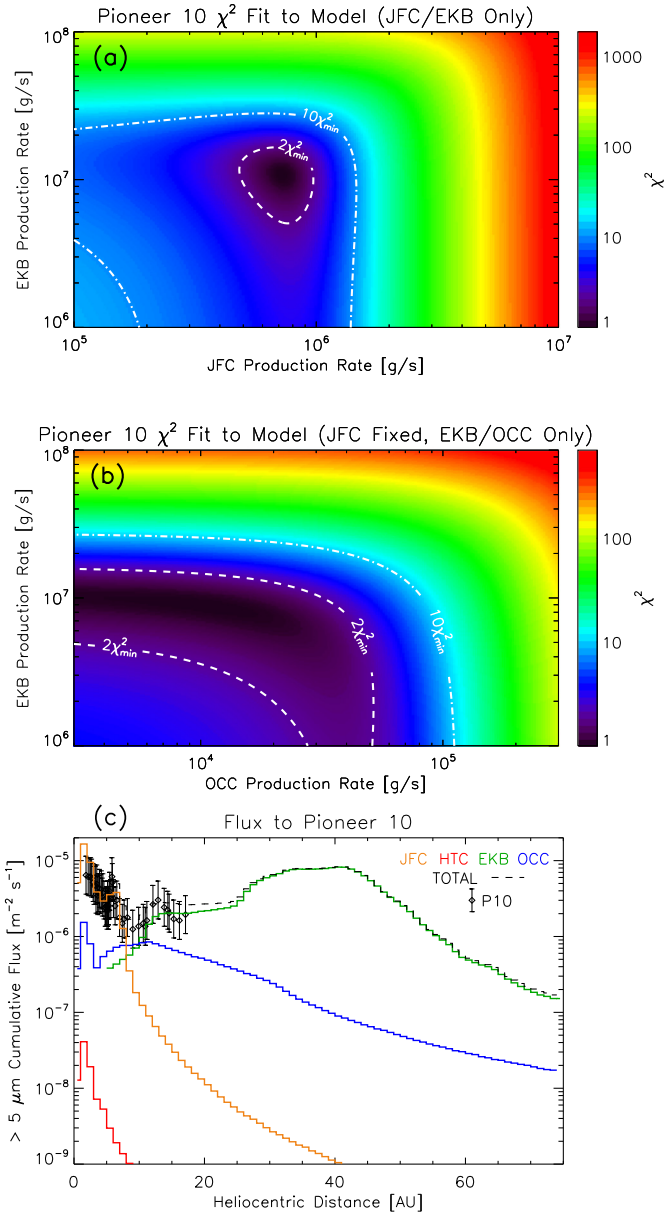

Fig. 4. (a) and (b) The χ^2 goodness-of-fit results for *Pioneer* 10 data-model comparison, as described in the text. (c) Best-fit model fluxes compared to *Pioneer* 10 flux measurements from Landgraf et al. (2002).

Fig. 4 shows the results of the χ^2 goodness-of-fit calculation for *Pioneer* 10. For this calculation, we chose to first fit the data to only JFC and EKB fluxes, as Nesvorný et al. (2010) have shown that JFC fluxes must dominate in the inner Solar System and EKB fluxes should dominate for the far outer Solar System. The results of the JFC-EKB fit are shown in Fig. 4(a) as a color contour of the χ^2 value relative to the minimum. For this fit, we find a well defined, local minimum for both the JFC and EKB productions rates at $N_{p,JFC} = 0.7 \times 10^6$ g/s and $N_{p,EKB} = 1.1 \times 10^7$ g/s. For reference, we also plot the $2 \times \min(\chi^2)$ and $10 \times \min(\chi^2)$ contours as dashed and dot-dash lines, respectively. In order to also constrain the possible contribution of OCC grains, which Nesvorný et al. (2010) have suggested contribute <10% to the interplanetary dust density, we have conducted a second χ^2 goodness-of-fit test, with the JFC production rate frozen at the best-fit value from the first test and allowing only the EKB and OCC production values to vary. The results of this test are shown in Fig. 4(b). For this case, the best-fit EKB production rate is approximately 10^7 g/s. OCC production rates higher than $\approx 5 \times 10^4$ g/s can be immediately ruled out as the χ^2 value rapidly rises (indicating a poorer fit) for higher OCC production rates, while lower production rates (even down to zero) are feasibly allowed by the χ^2 fit. Interestingly, the maximum value allowed by the χ^2 fit for the OCC production rate, $\approx 5 \times 10^4$, is roughly 10% of the best-fit JFC production rate, well in line with the findings of Nesvorný et al. (2010), and thus, we adopt this OCC production rate in our best-fit model (see Table 2). It should be emphasized, however, that this adopted production rate is an upper limit and future observational constraints (e.g., *Cassini* dust measurements at Saturn) may place more stringent limits on this value.

Fig. 4(c) shows a comparison of the data and best-fit model values for the >5 μm flux to *Pioneer* 10 as a function of heliocentric distance. The modeled fluxes are a mixture of JFC, OCC, and EKB grains, with each family contributing to the observed fluxes at varying levels as a function of heliocentric distance. Inside of approximately 7 AU, JFC grains dominate the P10 flux while OCC grains contribute roughly 10%. Between 7 and 15 AU, a mixture of JFC, OCC, and EKB grains contribute at nearly equal levels to the observed flux. Beyond 15 AU, JFC and OCC grains both decline

Table 2
Dust production rate constraints from the χ^2 goodness-of-fit tests to both SDC and *Pioneer* 10 data.

Dust grain family	0.1–10 μm Production rate [g s^{-1}]	Mass dist. slope ($dM \propto m^{-\alpha/3}$)
Edgeworth-Kuiper Belt (EKB)	6×10^6–1×10^7	$\alpha = 2.5$
Jupiter-family comets (JFC)	0.7×10^6	$\alpha = 2.5$
Oort-Cloud comets (OCC)	$< 5 \times 10^4$	$\alpha = 2.5$
Halley-type comets (HTC)[a]	$< 1 \times 10^4$	$\alpha = 2.5$

[a] The HTC production rate is estimated to be no larger than ≈1% of JFC grains based on Nesvorný et al. (2010).

while EKB grains become the dominant source of flux. We also have plotted a 1% contribution from HTCs based on the constraints of Nesvorný et al. (2010), shown in red, which do not appreciably contribute at all to the P10 flux. The roughly equal contribution of various dust grain sources to the observed P10 meteoroid flux matches the conclusion drawn previously by Landgraf et al. (2002), who modeled dust grains from three sources: comet 29P/Schwassman-Wachmann-1 (similar to JFC grains in our model), comet 1P/Halley (HTC grains), and the Edgeworth-Kuiper Belt (EKB grains). We note that results of Nesvorný et al. (2010) would suggest that the HTC grains do not significantly contribute to P10 fluxes as used in Landgraf et al. (2002); rather, the OCC grains provide an additional source of cometary flux to P10.

For SDC, whose measurements span from approximately 5 AU to 30 AU (neglecting the inner Solar System measurements reported by Poppe et al. (2010)), we fit the results to EKB grains only. This choice is motivated by simple inspection of the flux curves as a function of heliocentric distance. The cometary sources all drop steeply as a function of heliocentric distance while only the EKB grains are relatively flat, similar to the data. The results of the SDC χ^2 fit are shown in Fig. 5(a). The χ^2 curve has a minimum at $N_{p,EKB} \approx 6 \times 10^6$ g/s, only a factor of approximately two different than the independently obtained EKB production rate from *Pioneer* 10 data. Fig. 5(b) shows the best-fit flux from the model compared to the SDC data as a function of heliocentric distance, where we have used the best-fit production rates for JFC and OCC grains obtained from the *Pioneer* 10 fit. The model shows an excellent fit to the SDC data, with the exception of two points between 5 and 10 AU. EKB grains dominate the SDC flux over all other species throughout the Solar System at fluxes of approximately 5×10^{-4} m^{-2} s^{-1}. JFC grains contribute approximately half the flux of EKB grains at 5 AU, but rapidly drop off as a function of heliocentric distance. OCC grains contribute to the observed SDC fluxes at a maximum of only 10% at 5 AU, and also decline as a function of distance. HTC grains contribute <1% and are not shown in Fig. 5(b). Finally, Table 2 summarizes the resulting best-fit production rate (characterized as the production rate of 0.1–10 μm grains), for each family, as determined by the χ^2 fits to both SDC and *Pioneer* 10.

3.5. Fluxes to the outer planets

Using the production values derived for each dust family summarized in Table 2, we compute the density and flux to an object on a circular orbit as a function of heliocentric distance, shown in Fig. 6. The density of 2 μm and 5 μm grains, panels Fig. 6(a) and (b), respectively, are constant within one order of magnitude throughout nearly the entire Solar System. Densities inside 5 AU are dominated by JFC grains while EKB grains dominate outside 5 AU. OCC grains contribute to the 2 μm and 5 μm grain density around 5–10 AU yet are much less than the EKB density beyond 10 AU. As the grain size increases, the JFC density dominates increasingly over the other populations inside of 10 AU while the EKB grains dominate significantly outside 10 AU (the exception

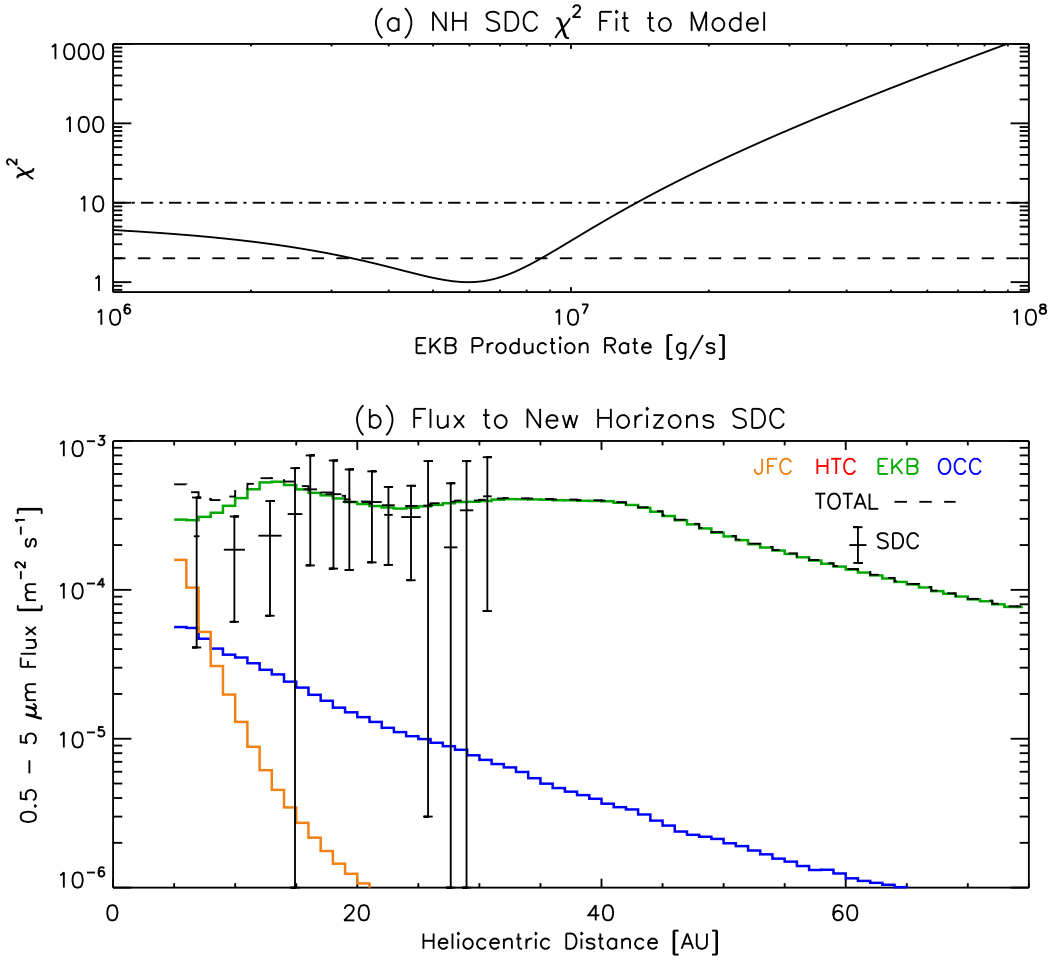

Fig. 5. (a) The χ^2 goodness-of-fit results for SDC data-model comparison. (b) Best-fit model fluxes compared to SDC flux measurements from Poppe et al. (2010) and Szalay et al. (2013).

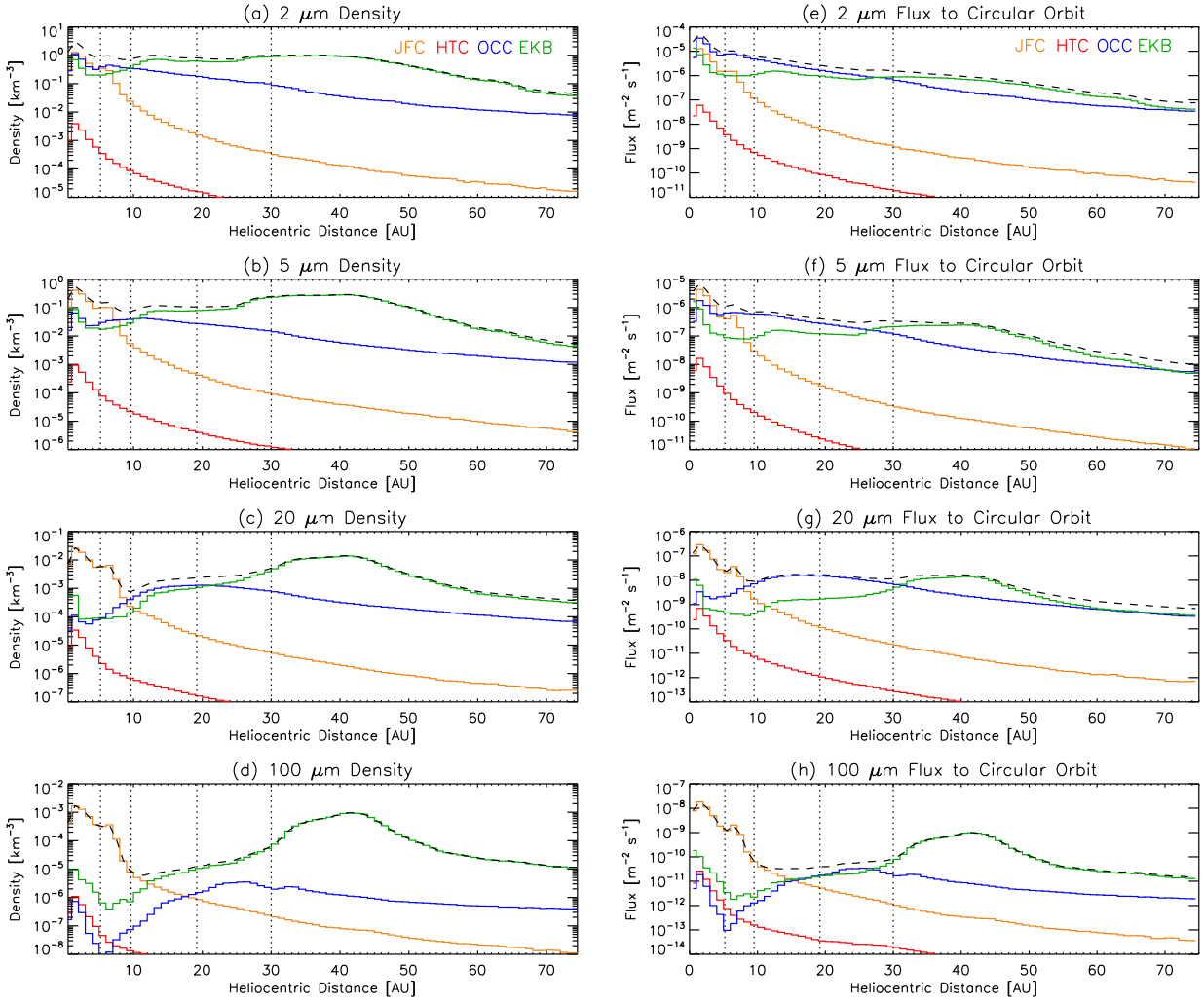

Fig. 6. The densities (a–d) and fluxes (e–h) of 2, 5, 20, and 100 μm grains as a function of heliocentric distance. Fluxes are computed to objects on a local, circular keplerian orbit.

being for ≈20 μm OCC grains which have similar density to EKB grains between 10 and 20 AU). Across all sizes, HTC grains contribute only a trace amount of density. The dust grain flux to a circular orbit shows somewhat different trends than the density due to differing velocity distributions between the populations (see Section 3.2 and Fig. 3). For example, OCC grains between 2 and 20 μm have fluxes greater than that from EKB grains between approximately 5 and 30 AU, despite having lower densities. This increase is governed by the OCC grain velocity distribution (see Fig. 3) which is much higher in magnitude due to the very high eccentricity of the parent OCC bodies compared to the EKB objects. What is most evident from the fluxes in Fig. 6 is that multiple sources of dust grains can contribute to the flux to an object in the outer Solar System depending on the orbital distance and dust grain size, rather than a single population that is easily extrapolated in either grain size and/or distance.

By summing over masses, we can compute the 0.5–100 μm interplanetary dust grain mass flux to objects on circular orbits, assuming no gravitational focusing, as a function of heliocentric distance, shown in Fig. 7. The total mass flux over all dust grain sources is shown as the dashed line, with individual contributions in color. JFC grains comprise a majority of the flux within 10 AU, followed by OCC grains between 10 and 25 AU, and EKB grains outside of 25 AU. Notably, the flux drops steeply as a function of heliocentric distance from the inner Solar System out to 10 AU. The flux from OCC grains remains relatively flat between 5 and 30 AU and contributes significantly to mass fluxes at Saturn, Uranus, and Neptune. Finally, the mass flux has a broad secondary peak at approximately 40–42 AU in the heart of the Edgeworth-Kuiper Belt. We also plot two comparisons: (1) the dash-dot line shows the Grün et al. (1985) interplanetary dust flux for radii between 0.5 and 100 μm, extrapolated from 1 AU assuming that the flux scales as $r^{-0.5}$ (equivalent to assuming a constant dust density and radially decreasing heliocentric velocity), and (2) the upside-down triangle denotes the inferred 0.5–100 μm mass flux into the jovian system (note that the 0.5–100 μm is estimated to be roughly half the total mass flux reported in Sremčević et al. (2005)). We also note that the inferred mass flux at Jupiter derived by Sremčević et al. (2005) is uncertain to roughly an order-of-magnitude due to uncertainties in the ejecta yield and assumptions made about the incoming interplanetary dust grain velocity distribution.

Based on the *Pioneer* 10 and SDC in situ constraints, the model underestimates the mass flux to Jupiter in comparison to the Sremčević et al. (2005) 0.5–100 μm inferred flux by approximately a factor of four. Considering the $2 \times \chi^2$ contours from Fig. 4 as a measure of the fit uncertainty, we find that the maximum mass flux to Jupiter within error bars is approximately 1.0×10^{-13} g m^{-2} s^{-1} compared to the Sremčević et al. (2005) flux of 1.5×10^{-13} g m^{-2} s^{-1}. We tested the sensitivity of the flux at Jupiter as a function of

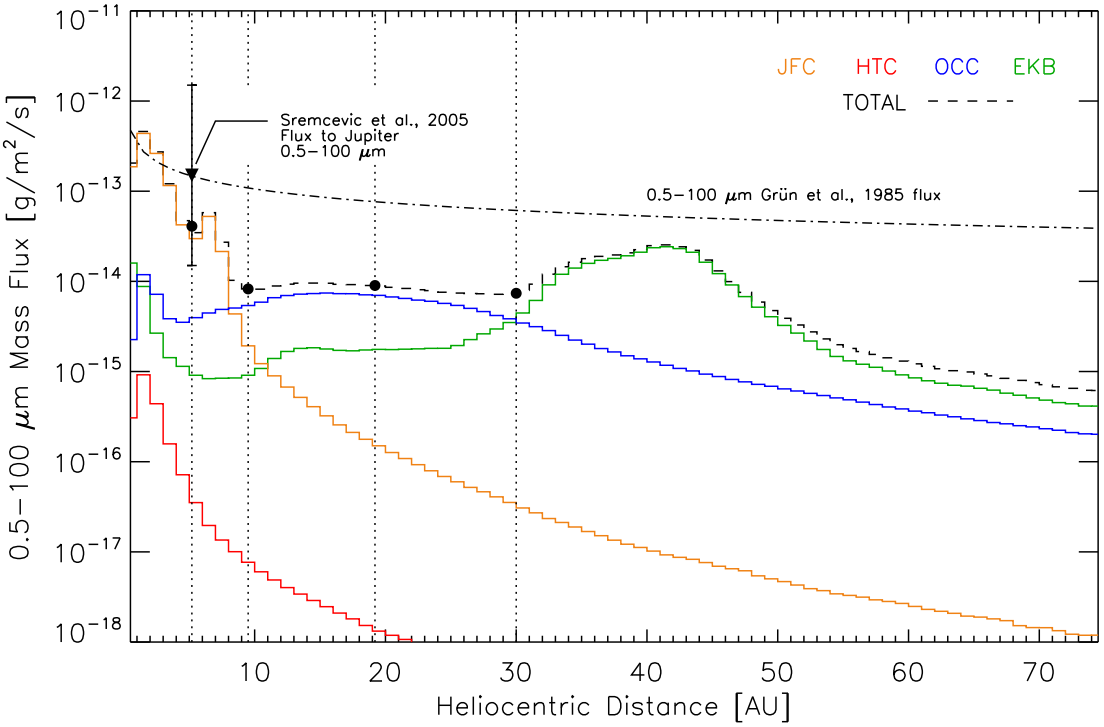

Fig. 7. The 0.5–100 μm unfocused mass flux [g m^{-2} s^{-1}] as a function of heliocentric distance, shown as the total (dashed line) and as contributions from each dust grain species (colored lines). The upside-down triangle marks the inferred 0.5–100 μm IDP flux at Jupiter from Sremčević et al. (2005), the dash-dot line is the 0.5–100 μm flux from Grün et al. (1985), scaled as $r^{-0.5}$, and the solid circles denote 0.5–100 μm unfocused mass flux to each of the giant planets from the best-fit model results (c.f., Table 2). (For interpretation of the references to color in this figure legend, the reader is referred to the web version of this article.)

the mass distribution slope, α, for JFC grains, since they dominate the flux to Jupiter. A shallower slope (i.e., $\alpha < 2.5$) would allow for a better simultaneous fit of both the *Pioneer* 10 and SDC data and the 0.5–100 μm flux at Jupiter. Indeed, we found that a value of $\alpha \approx 2.0$ for JFC grains achieves such a simultaneous agreement. In truth, we find that such a change to the JFC production slope is somewhat arbitrary and that the disagreement between the modeled flux and the Sremčević et al. (2005) inferred flux is more likely a factor of uncertainties in one of several places, including the *Pioneer* 10 and SDC in situ measurements, the Galileo measurements, or the dynamics of dust grains in our model (i.e., collisional products, grain densities, etc.).

Applying the in situ SDC and *Pioneer* 10 constraints, the model makes a significant prediction: namely, that the fluxes to Saturn, Uranus, and Neptune are at least an order-of-magnitude *less* than that expected from a simple extrapolation of dust grain flux models for the inner Solar System (e.g., Grün et al., 1985) and possibly lower, since the OCC contribution is only an upper limit. The flux of JFC grains decreases faster than $r^{-0.5}$ as would be expected for the assumption of a constant density (i.e., the heliocentric velocity scales as $r^{-0.5}$). Furthermore, the flux provided by both OCC and EKB grains outside of Jupiter's orbit is insufficient to bring the interplanetary dust grain mass fluxes up to the extrapolated values. This depletion in mass flux is mainly driven by lower fluxes at higher grain masses ($a \sim 100$ μm) as opposed to smaller grains that are directly measured by both SDC and *Pioneer* 10 and remain relatively constant in flux in the outer Solar System.

3.6. Gravitational focusing and planetary fluxes

While Fig. 7 shows model results for dust fluxes at the Hill radius of each of the outer planets, it is important to take into account the role of gravitational focusing in enhancing the dust flux within each planetary system. As dust grains enter a planetary system, the local gravitational force accelerates the grains and increases the overall magnitude of the flux by a factor of,

$$G(r) = \sqrt{1+\frac{v_{esc}(r)^2}{v_\infty^2}}\left[\frac{1}{2}\sqrt{1+\frac{v_{esc}(r)^2}{v_\infty^2}} + \frac{1}{2}\sqrt{1+\frac{v_{esc}(r)^2}{v_\infty^2}-\frac{R_p^2}{r^2}\left(1+\frac{v_{esc}(r)^2}{v_\infty^2}\right)}\right], \quad (4)$$

where r is the distance from the central body, R_p is the planetary radius, $v_{esc}(r)$ is the escape speed at distance r, and v_∞ is the dust grain speed at infinity (Spahn et al., 2006). Note that in the limit of $r \gg R_p$, this expression reduces to that derived in Colwell (1994); however, for $r \sim R_P$, the solution diverges from the Colwell (1994) approximation by up to a factor of two. Slower grain populations at the planet's Hill radius will experience higher flux increases due to gravitational focusing. The combination of several dust grain sources each with different speed distributions (see Fig. 3) at the Hill radius implies that the relative combination of fluxes from different sources may change at each planet as a function of planetary radial distance.

At each planet, for each grain type (EKB, JFC, OCC, HTC) and size, we have calculated the gravitationally focused flux as a function of distance from the planet. Fig. 8 shows the 0.5–100 μm gravitationally focused mass flux as a function of distance for each dust grain source at each planet. In many cases, the increase in flux due to focusing can be over an order-of-magnitude. At Jupiter, both the JFC and EKB fluxes are heavily focused ($\approx 100\times$) due to their low relative impact speed while the OCC grains gain only a factor of two. JFC grains dominate the flux throughout the jovian system including at the four Galilean satellites. At Saturn, the EKB and JFC populations are focused the most and the OCC population is focused only slightly. By coincidence, each of these three sources

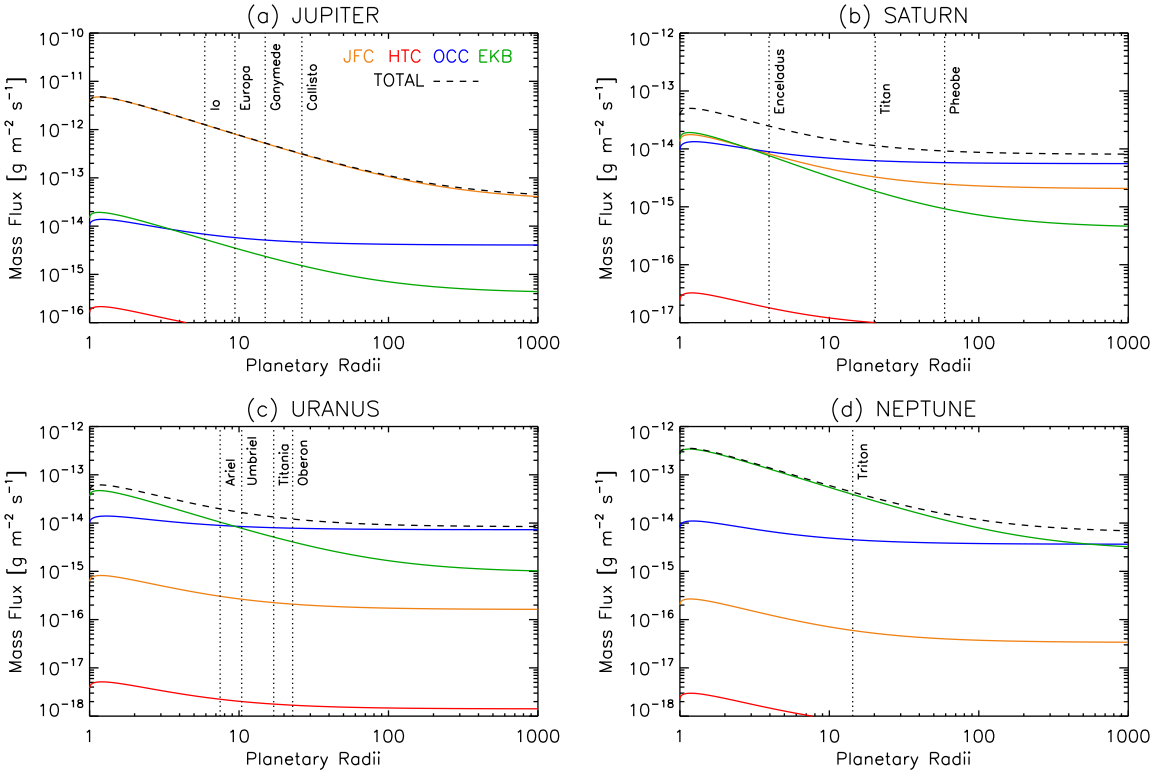

Fig. 8. The 0.5–100 μm focused mass flux at each outer planet as a function of radial distance from the planet center. Individual dust families are marked in color, with the total mass flux denoted by the dashed line. At each planet, locations of some relevant satellites are noted. (For interpretation of the references to color in this figure legend, the reader is referred to the web version of this article.)

have nearly identical fluxes at one Saturn radius. OCC flux tends to dominate outside of the orbit of Enceladus (≈4 R_S), with a nearly equal mixture of EKB, JFC, and OCC flux inside the orbit of Enceladus. At Uranus, EKB grains are most heavily focused (≈80×), while OCC, JFC, and HTC grains have smaller focusing factors. OCC fluxes, which are dominant at the Hill radius by almost an order-of-magnitude over EKB grains, dominate the flux outside ≈10 R_U, within which they are overtaken by the focused EKB flux. Finally, at Neptune, EKB and OCC grains represent nearly equal fluxes at the Hill radius, yet due to the very low impact speed of EKB grains compared to OCC grains at Neptune, the EKB grains are heavily focused and represent the dominant IDP flux within the neptunian system.

4. Comparison to atmospheric oxygen influx constraints

Feuchtgruber et al. (1997, 1999), using observations by the *Infrared Space Observatory* (ISO), reported the surprising presence of water vapor and carbon dioxide in the atmospheres of Jupiter, Saturn, Titan, Uranus, and Neptune. Given that H_2O condenses deep in the tropospheres of the giant planets and that upwelling of oxygen species from the deep interiors of the giant planets is expected to be inefficient, this argued strongly in favor of the delivery of oxygen (possibly in the form of H_2O, CO, or CO_2) from exogenous sources. These exogenous sources include direct cometary impact, such as the Shoemaker-Levy 9 impact at Jupiter (e.g., Zahnle and Mac Low, 1994; Orton et al., 1995), planetary ring or satellite debris and neutrals, such as the E-ring and neutral torus at Saturn (Jurac and Richardson, 2007; Cassidy and Johnson, 2010; Fleshman et al., 2014), or ablation of interplanetary dust grains (e.g., Moses, 1992, 1997). With the calculations of gravitationally-focused interplanetary dust fluxes to each of the outer planets, Fig. 8, we can compare to oxygen influx rates inferred from a combination of infrared observations and associated photochemical modeling. We take the gravitationally focused mass flux at one planetary radius for each outer planet and assume that oxygen comprises half of the total dust composition by number for typical dust grain compositions (Jessberger and Kissel, 1991), although variability in this fraction has been observed in the composition of other cometary ejecta and extrasolar debris disks (i.e., Lisse et al., 2006, 2007b).

Fig. 9 compares the net oxygen influx of interplanetary dust grains predicted from this model (black) with various observational and photochemical modeling based constraints for each of the outer planets. For our model, we have roughly assumed an order-of-magnitude uncertainty, since the various sources of error from both the model assumptions and the fits to the data are difficult to quantitatively combine. At Jupiter, our model predicts a net O number influx from IDP ablation of approximately 1×10^7 cm^{-2} s^{-1}. In comparison, Lellouch et al. (2002) have placed an extremely stringent upper limit on H_2O influx to Jupiter of $< 8 \times 10^4$ cm^{-2} s^{-1} and Bézard et al. (2002) have placed oxygen influx limits at $1.5 - 10 \times 10^6$ cm^{-2} s^{-1} from observations of CO. The upper limit on H_2O influx from Lellouch et al. (2002) is rather surprising given that the IDP flux at Jupiter is perhaps the best constrained from among the outer planets given the in situ measurements by the Galileo DDS instrument (Krivov et al., 2003; Sremčević et al., 2005). Various possibilities for the apparently large CO/H_2O deposition ratio at Jupiter have been considered by Bézard et al. (2002), including a compositional difference in grains ablating in Jupiter's atmosphere, efficient production of CO during grain ablation at Jupiter due to higher incoming velocities, and finally, the impact of km to sub-km sized comets, which are known to more efficiently produce CO from available oxygen via shock chemistry (Zahnle, 1996). We note that our model predicts that Jupiter receives nearly all of its IDP flux from a single source,

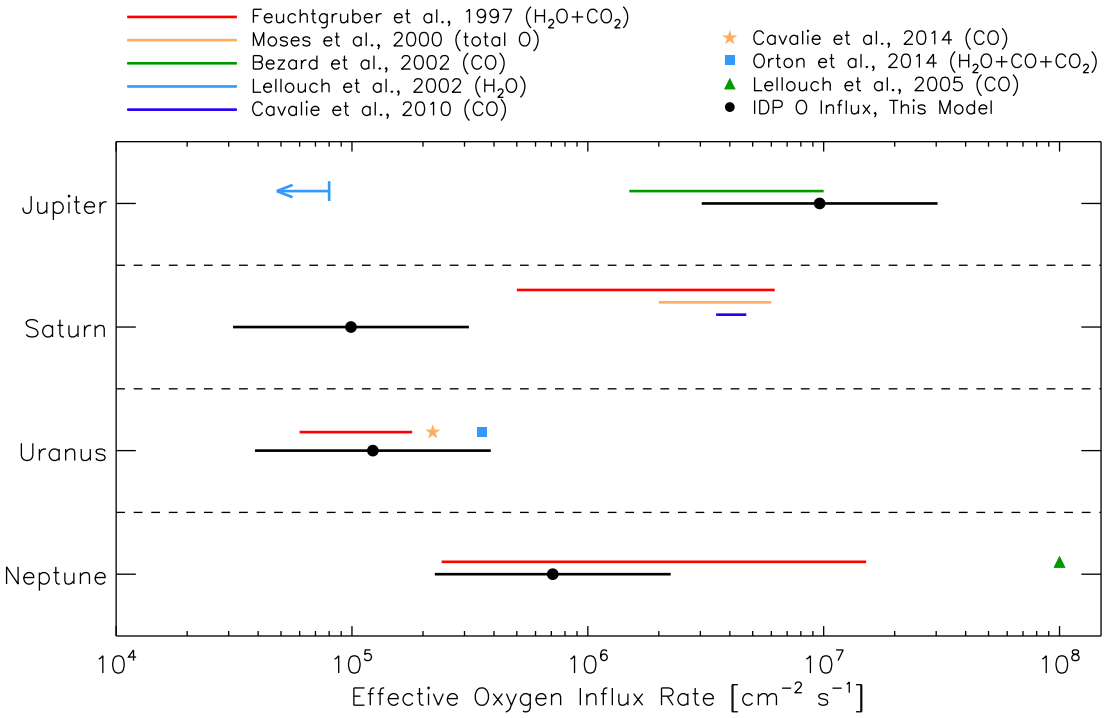

Fig. 9. A comparison of equivalent oxygen number flux predictions from this model (black) with various constraints on oxygen influx to each outer planet based on observations and photochemical modeling.

namely the Jupiter-family comets, while the other giant planets have IDP influx dominated by Oort-Cloud cometary grains and EKB grains. Despite this, fundamental IDP grain compositional differences of the order necessary to produce a CO/H_2O deposition ratio consistent with Bézard et al. (2002) ($CO/H_2O \approx 30$) are hard to consider seriously, even though varying C/O ratios in cometary dust have been observed (e.g., Lisse et al., 2007b). Compositional differences between JFC and EKB dust are also hard to envision since JFCs are thought to be EKB objects themselves that have "leaked" into the outer Solar System (Levison and Duncan, 1997). Favorable production of CO over H_2O during IDP ablation may be possible due to the higher relative atmospheric impact velocities at Jupiter compared to the other giant planets (since CO production is favored at higher temperatures), yet Bézard et al. (2002) rightly note that the temperature difference is relatively modest. In sum, the only way to satisfy both the IDP influx rates presented here and the low H_2O influx constraints of Lellouch et al. (2002) is for the incoming oxygen to be efficiently converted to CO or sequestered as metal oxides or silicates, yet there are currently no available models for the immediate fate of the ablated species in the meteor trail with which to validate this theory.

At Saturn, we predict an oxygen influx of approximately 1×10^5 cm^{-2} s^{-1}. Observations put the oxygen influx to Saturn's atmosphere at more than an order-of-magnitude higher near 4×10^6 cm^{-2} s^{-1} (Feuchtgruber et al., 1997; Moses et al., 2000; Cavalié et al., 2010). This difference is not entirely surprising given the injection of water ice and gas from Enceladus, which dominate the influx of water to Saturn's atmosphere (i.e., Cassidy and Johnson, 2010; Fleshman et al., 2014), although, "ring rain" from Saturn's main ring system (Moore et al., 2015) or direct cometary impacts (Cavalié et al., 2010) may also contribute substantial amounts of oxygen to the atmosphere. While not shown in Fig. 9, our model predicts an oxygen influx from interplanetary dust grain ablation to the atmosphere of Titan of approximately 4×10^4 cm^{-2} s^{-1}, nearly an order-of-magnitude less than that required from analysis and photochemical modeling of Herschel observations of water vapor in Titan's atmosphere (Moreno et al., 2012). Thus, a similar conclusion can be drawn for Titan as for Saturn, namely, that Enceladus-originating water vapor most likely dominates the oxygen influx to Titan.

The observed flux of exogenous oxygen to Uranus is consistent with a dominant source from ablation of interplanetary dust, with our prediction of 1.2×10^5 cm^{-2} s^{-1} agreeing with the Feuchtgruber et al. (1997) H_2O/CO_2, Cavalié et al. (2014) CO, and Orton et al. (2014) $H_2O/CO/CO_2$ results. Cometary impacts must certainly deliver some oxygen to the atmosphere of Uranus similar to that seen at Jupiter (e.g., Zahnle and Mac Low, 1994; Orton et al., 1995) and suspected at Neptune (Lellouch et al., 2005; Hesman et al., 2007; Luszcz-Cook and de Pater, 2013); however, if interplanetary dust grain ablation is currently providing the bulk of external oxygen to Uranus, then one can estimate the length of time since the most recent cometary impact. If we assume that cometary impact produces predominantly CO, use an eddy diffusion coefficient of $K_{zz} = 2400$ cm^2 s^{-1} (Orton et al., 2014), and estimate the distance between the splash-back region of the cometary impact (≈ 0.01 mbar) and the tropopause to be $d \approx 350$ km, then the diffusion time for CO to reach the tropopause is $\tau \approx d^2/K_{zz} \approx 16,000$ yr. This timescale is significantly longer than that calculated for mean cometary impact times from Levison and Duncan (1997), who estimated an impact rate of 1.3×10^{-3} yr^{-1}, or one comet every 700 years. Thus, it seems entirely likely that both interplanetary dust grains and direct cometary impacts may deliver appreciable amounts of oxygen-bearing species to the atmosphere of Uranus.

At Neptune, our model predicts an oxygen influx of 7×10^5 cm^{-2} s^{-1}, which is in line with constraints of H_2O influx from Feuchtgruber et al. (1997), yet is two orders-of-magnitude less than that required for CO abundance by Lellouch et al. (2005). While not shown on Fig. 9, Hesman et al. (2007) have put forth an even higher CO influx requirement of nearly

1×10^{10} cm^{-2} s^{-1} based on more recent observations by the James Clerk Maxwell Telescope (JCMT). Such a discrepancy between the H_2O and CO influx to Neptune, as well as the derived vertical profile for the CO, which shows the bulk of the CO to be confined at relatively high altitudes (i.e., it has not diffused into the lower stratosphere), is thought to be strong evidence for a recent cometary impact in the atmosphere of Neptune, since CO is more efficiently produced via shock chemistry upon cometary impact than during meteoroid ablation (Zahnle, 1996) and has not yet diffused into and condensed in the troposphere. While interplanetary dust grains will ablate and serve as a source for both H_2O and CO, the very high CO/H_2O ratio implies the need a greater source of CO. We interpret the comparably low oxygen influx from IDPs at Neptune relative to that required from atmospheric observations as further supporting evidence of a "recent" cometary impact at Neptune (i.e., Lellouch et al., 2005; Hesman et al., 2007; Luszcz-Cook and de Pater, 2013).

5. Discussion and conclusion

The model presented here is an important step towards fully understanding the interplanetary dust environment in the outer Solar System. The model builds on improvements in the ability to model the physics of interplanetary dust grain dynamics, the availability of in situ and remote-sensing constraints, and recent updates in our knowledge of the distributions of dust grain parent bodies (i.e., Appendix A). By including the grain–grain collisional algorithm introduced by Stark and Kuchner (2009), we have more accurately modeled the distribution and flux of EKB grains specifically. We have confirmed their results that these collisions play a significant role in re-shaping the EKB dust disk and must be accounted for in all future models. While we have not at this time included collisions either within or between the other populations (JFC, OCC, HTC), we know that they most likely play some role in altering the equilibrium density distributions for these species. At 1 AU, Grün et al. (1985) have calculated that the particle collisional time is equal to the Poynting–Robertson drag time for grains with $m \approx 10^{-5}$ g (≈ 100 μm). Grains smaller than this drift into the Sun faster than they can be collisionally destroyed while larger particles cannot. In the outer Solar System, the (typically) lower dust fluxes imply that collisional frequencies would decline; however, Poynting–Robertson drag lifetimes also increase proportional to the initial semi-major axis of a dust grain (Wyatt and Whipple, 1950), and thus, collisions may still play an important role in shaping the OCC and JFC density distributions in the outer Solar System (as also noted by Nesvorný et al. (2010, 2011)). Future development of the model will couple all sizes and types of dust grains in a fully self-consistent collisional algorithm.

Our model predicts that dust grain fluxes to the outer planets are typically a mixture of grains from different sources, with the exception of Jupiter, which is dominated by the influx of Jupiter-family comet grains. Saturn appears to sit at the threshold where JFC, EKB, and OCC grains all contribute within one order-of-magnitude of each other, while Uranus and Neptune have contributions mainly from EKB and OCC grains (noting again that the OCC contribution is only an upper limit and may be lower). Distances beyond Neptune, i.e., the Edgeworth-Kuiper Belt itself, are dominated by EKB grains with 0.5–100 μm mass fluxes only slightly lower than that at 5 AU. Also of importance is the discrepancy between our model and the extrapolated Grün et al. (1985) interplanetary dust flux. The model disagreement is not surprising, given that the sources and dynamics of dust grains in the outer Solar System are significantly different than those at 1 AU. While such an extrapolation has been necessary given the long-persisting uncertainties in outer planetary dust fluxes, the model presented here shows that more accurate estimates of dust influxes to the outer planets are now available.

Our model will continue to be tested by the *New Horizons* Student Dust Counter, which will return to making routine dust flux measurements after the Pluto encounter of mid-2015 (Horányi et al., 2008; Stern, 2008). As SDC continues out of the Solar System, the measured fluxes should remain constant until approximately 45 AU, at which point they begin to decrease. This is in contrast to the flux predicted by Vitense et al. (2014), who predicted that SDC should measure a "clump", or increase, in the 0.5–5 μm flux centered around 30 AU up to approximately 10^{-3} m^{-2} s^{-1}. The difference may be partially due to different collisional algorithms used here and in Vitense et al. (2014). Here, grains are allowed to collide with any other size grain, while in Vitense et al. (2014), grains are limited to only collide with those of the same size. On the other hand, Vitense et al. (2014) allows for collisional *production* of grains, while we do not consider such a source at this time. Nevertheless, the true test for the presence of such "clumps" is in the data itself. SDC data out to 30 AU have not indicated the presence of such structures. Future measurements in the upcoming years will reveal whether any such structures exist further out. Our model also predicts that *Pioneer* 10 would have observed a nearly fivefold increase in the IDP flux between approximately 25 and 45 AU (see Fig. 4), had the instrument not ceased working at 18 AU.

Additional in situ constraints on the model can be imposed through the analysis of *Cassini* Cosmic Dust Analyzer (CDA) data at Saturn (Srama et al., 2004). While *Cassini* CDA made measurements of interplanetary dust fluxes during the cruise portion of the mission between Jupiter and Saturn and found both bound, prograde dust grains (assumed to be from a cometary source such as the JFC) and interstellar dust grains (Altobelli et al., 2007), the somewhat poor statistics prevent a rigorous comparison with our model. CDA measurements taken in orbit around Saturn, however, do have the ability to add important additional data to the model. Preliminary analysis of the CDA data have shown the ability to detect exogenous dust particles at Saturn with CDA (Kempf et al., 2013), and continued analysis will hopefully provide more stringent constraints on the dust influx to Saturn and in turn further advance our knowledge of dust densities and fluxes throughout the outer Solar System.

Finally, we have used the model-predicted influx of interplanetary dust grains to each outer planetary system to estimate the flux of exogenous oxygen to each of the outer planet atmospheres. Starting with Neptune, we find that while the oxygen delivered by interplanetary dust is in agreement with H_2O delivery estimates from Feuchtgruber et al. (1997), the delivered oxygen is several orders of magnitude smaller than that required to produced the observed CO in the atmosphere (Lellouch et al., 2005; Hesman et al., 2007; Luszcz-Cook and de Pater, 2013). We interpret this as further evidence of CO generation due to a large, recent cometary impact. At Uranus, oxygen influx from IDPs matches well with inferred steady source influxes from observational constraints (Feuchtgruber et al., 1997; Cavalié et al., 2014; Orton et al., 2014), yet impact rate studies for the outer Solar System would also suggest that km and sub-km sized comets may deliver a nearly equal amount of oxygen (Levison and Duncan, 1997; Zahnle et al., 2003). At both Saturn and Titan, interplanetary dust influx contributes approximately one order-of-magnitude less oxygen than is required from observations (Feuchtgruber et al., 1997; Moses et al., 2000; Cavalié et al., 2010), further confirming the unique role that the Enceladus neutral water torus plays in hydrating the saturnian system and atmosphere (Jurac and Richardson, 2007; Cassidy and Johnson, 2010; Fleshman et al., 2014). The greatest discrepancy is found at Jupiter, where our modeled interplanetary dust flux is several orders-of-magnitude greater than water influx

constraints derived by Lellouch et al. (2002), yet in line with the CO observations by Bézard et al. (2002). Bézard et al. (2002) may be correct that the observed jovian CO is mainly delivered by km and sub-km sized comets; however, it is also possible that the oxygen from incoming interplanetary dust grains is efficiently converted to CO during or after the ablation process. Regardless, the oxygen from the incoming dust grains clearly does not end up as water in Jupiter's hydrogen-dominated atmosphere, and alternative fates for the oxygen components of the interplanetary dust grains must be considered.

Acknowledgments

The author gratefully acknowledges support from NASA's Planetary Atmospheres Program, Grant #NNX13AG55G. The author thanks M. Horányi, J.R. Szalay, J.I. Moses, and C.M. Lisse for useful and constructive discussions. The author also thanks S. Kempf and an anonymous reviewer for constructive comments that improved the manuscript.

Appendix A. Description of model dust grain sources

A.1. Edgeworth-Kuiper Belt (EKB)

Our understanding of the spatial, orbital element, size, and compositional distributions of the various sub-populations of EKBOs is an active and evolving research area and thus, it is important to update dust grain models with the latest information. The necessity of individually modeling dust production from each of the various EKBO sub-populations is driven by fundamental differences in the EKBO sub-population orbital element distributions that contribute to significant differences in the resulting micron and sub-micron sized dust distributions (i.e., Kuchner and Stark, 2010; Vitense et al., 2010; Han et al., 2011). Here, we use results from the Canada–France Ecliptic Plane Survey (CFEPS) of EKBOs conducted from 2003 until late 2009 and reported variously in Jones et al. (2006), Kavelaars et al. (2009), Petit et al. (2011), and Gladman et al. (2012). Specifically, we employ the model results from Petit et al. (2011), which are constrained by CFEPS observations.

There is an abundance of nomenclature with regards to various sub-populations of EKBOs, many of which have different interpretations depending on the author. Given this, as well as the complex nature of the EKBO distributions determined by Petit et al. (2011), we give a detailed description here of the sub-populations used in our model (essentially those from Gladman et al. (2008) and further detailed in Petit et al. (2011)). At the highest level, the EKB can be divided into three categories: Resonant, Scattered/Scattering, and Classical. Dynamically speaking, the Resonant population are those EKBOs currently in resonance with Neptune (i.e., 2:1, 3:2, etc.) and the Scattered/Scattering population are those objects currently undergoing or having undergone scattering (within 10 Myr) by Neptune, as determined by orbital integration simulations. (We note that the Scattering/ed population defined here is not the same as the Scattered parent population used in our previous work (Han et al., 2011; Poppe and Horányi, 2012; Poppe, 2015), but rather a more specific sub-set of EKBOs.) All other objects (i.e., those not in resonance or currently scattering off of Neptune), fall into the classical belt. The classical belt is further sub-divided into a fairly detailed set of sub-components as determined by Petit et al. (2011). The breakdown of the classical belt is governed by the semi-major axis, a, and eccentricity, e, of the EKBOs:

1. Inner classical belt: objects with $a > a_N$ and $a < 3:2$ Neptune MMR, where a_N is the semi-major axis of Neptune.
2. Main classical belt: objects with $a > 3:2$ Neptune MMR and $a < 2:1$ Neptune MMR.
3. Outer classical belt: objects with $a > 2:1$ Neptune MMR and $e < 0.24$.
4. Detached classical belt: objects with $a > 2:1$ Neptune MMR and $e > 0.24$.

The eccentricity cutoff between the outer and detached belts ($e = 0.24$) is an arbitrary distinction as noted by Gladman et al. (2008); thus, similar to Petit et al. (2011), we group the outer and detached components together (and for simplicity, refer to this as just the "outer" population). The main classical belt is further sub-divided into three components which are necessary to reproduce the observed CFEPS EKBO distributions. These sub-components include:

1. Kernel: A dense, low-inclination ($i < 10^\circ$), low-eccentricity ($e \approx 0.05$) population spanning semi-major axes of 43.8–44.4 AU.
2. Stirred: A low-inclination ($i < 10^\circ$), moderate-eccentricity ($0 < e < 0.15$) distribution spanning semi-major axes of approximately 42–47 AU.
3. Hot: A relatively higher-inclination ($0 < i < 35^\circ$), higher-eccentricity ($0 < e < 0.25$) population spanning semi-major axes of 40–47 AU.

These sub-components are those graphically shown in Fig. 4 of Petit et al. (2011). Using these observational constraints on the parent EKB distributions, we have constructed a model for the relative dust production rates from each EKB sub-population. These calculations, detailed below, represent an improvement upon simply taking the relative *number* distribution of EKB objects by considering the detailed physics of ejecta dust production (which depends on the relative EKB size distributions in addition to their number distributions).

A.1.1. EKB relative dust family production rates

While previous work has typically used the ratio of the *number* of EKB objects between different sub-populations as a proxy for the relative dust production rates, the information provided by Petit et al. (2011) regarding the size distributions of each EKB sub-population allows us to quantify relative dust production rates more accurately. Specifically, dust production rates from EKBOs (or indeed, any airless object) depend not only on the number of such objects, but also the total surface area available (i.e., cross-section) for incoming bombardment and ejecta production and the likelihood that impact ejecta can escape the local gravitational potential well of the target object. In addition to determining the relative orbital structure of the EKB, Petit et al. (2011) have also calculated de-biased population estimates as a function of luminosity, H. To translate the population greater than a given luminosity to that greater than a given diameter, we assume an albedo of 0.05. Assuming the size distribution of each sub-population is a power-law (allowing for the possibility that each sub-population may have different power-law exponents), we extrapolate the results of Petit et al. (2011) for each sub-population to obtain the cumulative size distribution, $N(>D)$, as a function of diameter from 5 to 500 km. The formula for the cumulative size distribution is given by,

$$\log_{10} N_i(D) = a_i + b_i D, \tag{A.1}$$

where D is the EKB diameter and a_i and b_i are coefficients for the ith EKB sub-population determined from Petit et al. (2011). We plot the distribution for each sub-component (seven in total) in Fig. A.1(a).

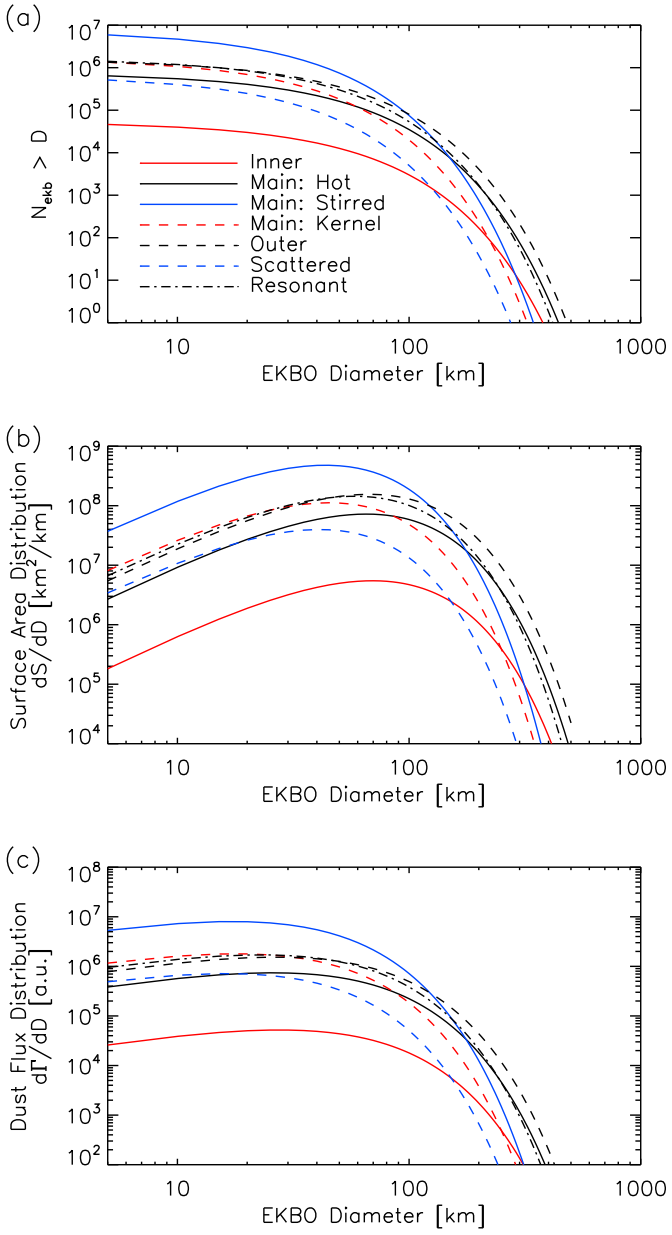

Fig. A.1. The (a) cumulative number distribution of EKB objects, (b) the differential surface area distribution, and (c) the differential dust flux production distribution, all as a function of the EKBO diameter shown for all seven EKBO sub-populations. Panels (a) and (b) are in physical units, while panel (c) is in arbitrary units.

The largest population by number is the main stirred component, with more than 5×10^6 objects greater than 5 km diameter. Other significant populations include the main kernel, outer, and resonant populations.

Starting with the cumulative size distribution, $N_i(d)$, for each population shown in Fig. A.1(a), we define the differential EKB size distribution as,

$$\frac{dN_i(D)}{dD} = A_i 10^{b_i D}, \tag{A.2}$$

where $A_i = 10^{a_i}$. Convolving this with the surface area as a function of diameter yields the differential surface area distribution, $dS_i(D)/dD$, given as,

$$\frac{dS_i(D)}{dD} = 4\pi D^2 \frac{dN_i(D)}{dD} \tag{A.3}$$

$$= 4\pi A_i b_i D^2 10^{b_i D} \tag{A.4}$$

Fig. A.1(b) shows the differential surface area distribution as a function of diameter for each sub-population with most distributions peaking between 50 and 100 km. While the available surface area does give a strong indication of the relative dust production, we must also account for the ability of freshly-created ejecta to escape the local gravitational potential of the parent EKBO. This in turn depends on the velocity distribution of the impact ejecta. Yamamoto and Mukai (1998), using cratering experiments and theory from a variety of sources (e.g., Housen et al., 1983; Lange and Ahrens, 1987; Frisch, 1992; Eichhorn and Grün, 1993), have derived the dependence of the escaping fraction of impact ejecta, f, on the escape velocity, v_{esc}, as either $f \propto v_{esc}^{-2}$ for hard, icy surfaces or $f \propto v_{esc}^{-1.21}$ for a layer of icy particles. If we adopt a layer of icy particles as the surface structure (given the likely surface gardening from impacting micrometeoroids), the differential flux of escaping ejecta from EKBs (i.e., those grains injected into the EKB dust disk), $d\Gamma_i(D)/dD$, as a function of EKB diameter can be derived as,

$$\frac{d\Gamma_i(D)}{dD} = D^{-1.21} \frac{dS_i(D)}{dD} \tag{A.5}$$

$$\propto A_i b_i D^{0.79} 10^{b_i D}. \tag{A.6}$$

The family of curves for each EKB sub-population is shown in Fig. A.1(c). For all populations, the curves are fairly broad between 5 and 200 km diameter, with much of the <200 km population contributing to EKB dust generation. Finally, in order to estimate the relative weight of each of the sub-populations with respect to EKB dust disk generation, we integrate each curve from 5 to 500 km and calculate the fraction that each sub-population contributes to the whole. These values are shown in Table A.3. The largest contributor to the EKB dust disk is the Main classical stirred population with 49%, followed by the main classical outer, resonant, and main classical kernel populations with 15%, 14%, and 11%, respectively. Smaller contributions come from the main classical hot, scattering/ed, and main inner populations with 7%, 4%, and 0.5%, respectively.

In order to reduce the complexity of our modeling, we have not separately modeled each of the seven EKB sub-populations, but rather only four, generally based on their orbital element groupings. First, we neglect the presence of the main inner population,

Table A.3
A comparison of the various sub-populations of the Edgeworth-Kuiper Belt and their relative contributions to the overall EKB interplanetary dust production rate.

EKB sub-population	Description	Fraction of EKB dust production
Main inner	$a_N < a < 3:2$;	0.005
Main classical hot[a]	$3:2 < a < 2:1$; $e < 0.25$; $i < 30°$	0.07
Main classical stirred[a]	$3:2 < a < 2:1$; $e < 0.25$; $i < 10°$	0.49
Main classical kernel[a]	$3:2 < a < 2:1$; $0.02 < e < 0.08$; $i < 10°$	0.11
Main outer	$a > 2:1$ with $f(a) \propto a^{-2.5}$;	0.15
Scattered/ing	Undergoing Neptune scattering within 10 Myr	0.04
Resonant	In resonance with Neptune	0.14

[a] See Petit et al. (2011) for a detailed description.

as this is projected to contribute <1% of the overall dust production. Our first population is taken as the main classical kernel population, as this population is unique in its confinement in orbital element space. For our purposes, we term this the "cold" EKB population, accounting for 11% of the overall dust production. Our second population combines those EKBOs that are dynamically "hot", which includes the main classical hot, main classical stirred, and scattered/ing, accounting for 60% of the overall production. Finally, we individually model both the main outer population (15%) and the resonant population (14%), as each of these has a unique orbital element structure. For the resonant subpopulation, we follow previous work and select individually known resonant EKBOs as source bodies. Thus, these four groupings (cold, hot, outer, and resonant) comprise the parent EKB populations used to seed our dust dynamics model, summarized in Table A.3.

A.2. Jupiter-family comets (JFC)

The second main source of dust grains included in the model are the Jupiter-family comets (JFC). Jupiter-family comets are objects believed to have migrated from the Edgeworth-Kuiper Belt under planetary gravitational scattering, passed through Centaur-like orbits, and finally, placed in near-Jupiter orbits with orbital periods typically less than 20 years (although this distinction is arbitrary). Levison and Duncan (1997) performed a series of Gyr dynamical simulations following EKB objects that were initially scattered by Neptune. The orbital element distribution of these simulated objects were found to be indistinguishable from the observed Jupiter-family comets, so long as the comets were recorded as active whenever their perihelion first dropped below 2.5 AU and that the comets had a median fading time of approximately 12,000 years. While these active JFCs are recognized as the main source of inner Solar System meteoroid streams (Jenniskens, 2006, 2008), they also must contribute to the dust density complex in the outer Solar System. Nesvorný et al. (2010) modeled dust dynamics of grains originating from JFCs (as well as several other asteroidal and cometary sources) and determined that JFCs are the dominant contributor to the interplanetary dust complex in the inner Solar System (≈90%) by comparison with mid-infrared imaging of the zodiacal cloud by IRAS (Hauser et al., 1984; Low et al., 1984). We follow the work of Nesvorný et al. (2010) by using orbital element distributions for JFCs derived from the simulations of Levison and Duncan (1997). These JFCs typically have semi-major axes smaller than that of Jupiter ($a_J = 5.2$ AU) and perihelia ranging from ≈0.5 to 4 AU. The inclination distribution is modeled as $dN(i) \propto \sin(i)\exp^{-0.5(i/\sigma_J)^2} di$, with $\sigma_J = 10^\circ$, approximating the results of numerical simulations by Levison et al. (2006) and Di Sisto et al. (2009). The argument of perihelion and longitude of ascending node are set to be uniform between $[0, 2\pi]$.

A.3. Oort-Cloud comets (OCC)

Oort-Cloud comets originate from the very edge of the Solar System and are remnant objects left over from the Solar System formation era (Oort, 1950). Orbital perturbations from passing stars and galactic tides will occasionally perturb an Oort-Cloud object onto an orbit with a perihelion within the planetary portion of the Solar System (<30 AU). Notably, a comparison of the observed distribution of dormant Oort-Cloud comets and dynamical simulations of the evolution of new OCCs (those comets on their initial perihelion passage) to returning (and possibly dormant) OCCs has demonstrated that a majority of OCCs must physically disrupt (Wiegert and Tremaine, 1999; Levison et al., 2002). As noted by Nesvorný et al. (2010), the physical disruption of OCCs must generate significant injections of cometary material into the Solar System. While much of this material may be ejected from the Solar System due to solar radiation pressure, some material could serve as an important source of interplanetary dust, both in the inner and outer Solar System. As discussed above for JFCs, Nesvorný et al. (2010) used observations of zodiacal cloud brightness obtained from the *Infrared Astronomical Satellite* (IRAS) to constrain the contribution of OCCs to the interplanetary dust complex. They found that their data are best fit if a small, ≈10%, contribution from OCCs are present; although, we do note that this contribution is somewhat uncertain and should be treated as an upper limit (Nesvorný et al., 2010).

Given the known outgassing and disruptive behavior of OCCs in the Solar System, combined with the constraints offered by Nesvorný et al. (2010), we include an OCC dust source in our model. Following previous work (Francis, 2005; Nesvorný et al., 2010, 2011), we model our initial OCC dust grains with a perihelion distribution of,

$$dN(q) = \begin{cases} 1 + \sqrt{q} & q < 2 \text{ AU} \\ 2.41(q/2)^{\gamma} & q > 2 \text{ AU} \end{cases}, \tag{A.7}$$

semi-major axes between 1000 and 10,000 AU, an inclination distribution of $dN(i) \propto \sin(i)$, and uniform longitude of ascending node and argument of perihelion. We note that while Francis (2005) found a perihelion distribution power-law index of $-0.5 < \gamma < 0.0$, yielding a distribution that declines slightly as a function of q, Nesvorný et al. (2010) used $0.0 < \gamma < 1.0$, which is a population that increases slightly in q. We tested two choices for the slope, $\gamma = -0.5$ and $\gamma = 0.5$, and found indistinguishable differences in the OCC dust grain density and velocity distributions, most likely due to a combination of the already weak power-law dependence on q and the rapid scattering of OCC grains by the giant planets, which tends to weaken the connection of dynamically evolving grains to their exact parent body distribution. For model results presented here, we used $\gamma = 0.5$. Similar to the JFCs, the longitude of ascending node and argument of perihelion are randomly distributed through $[0, 2\pi]$.

A.4. Halley-type comets (HTC)

Halley-type comets, named after the prototypical comet 1P/Halley, are characterized by orbital periods between 20 and 200 years. The full orbital element distribution of these comets is not well constrained, and thus, we follow previous work in generating initial conditions such that the parent bodies have periods, $20 < P < 200$ years, are weighted with perihelia $dN(q) \propto q$, and have an inclination distribution of $dN(i) \propto \sin(i)\exp^{-0.5(i/\sigma_H)^2} di$, where $\sigma_H = 30^\circ$ (Levison et al., 2006; Nesvorný et al., 2010). Longitude of ascending node and argument of perihelion are assumed to be uniformly random. We do note that Nesvorný et al. (2010) have shown that HTCs have only a minor contribution (<1%) to the interplanetary dust flux based on comparison to IRAS observations; nevertheless, we include this population in our modeling for completeness.

A.5. Other sources

Several other minor sources of dust grains exist in the outer Solar System. These potentially include Centaurs (Horner et al., 2004; Jewitt, 2009), Neptune Trojans, and interstellar dust grains (Grün et al., 1993). Centaurs have slightly varying definitions based on their orbital elements, but for simplicity's sake, Jewitt (2009) specified Centaurs as those non-resonant objects with both perihelion and semi-major axis between the semi-major axes of Jupiter and Neptune. These objects are essentially "leaking" out of the Edgeworth-Kuiper Belt, although the exact source of Centaurs from

within the EKB is not yet determined (e.g., Volk and Malhotra, 2008). Centaurs are on highly unstable orbits as they repeatedly interact gravitationally with the giant planets; indeed, some two-thirds are typically ejected from the Solar System into interstellar space (Tiscareno and Malhotra, 2003). The remaining one-third of Centaurs can become trapped in inner Solar System orbits, termed Jupiter Family comets (see Section A.2), where they sublimate and contribute massive amounts of dust to the interplanetary zodiacal cloud (Nesvorný et al., 2010). Some Centaurs are known to be active before dynamically reaching JFC status, including objects such as 39P/Oterma, (2060) 95P/Chiron, and (60558) 174P/Echelus, with dust production rates estimated between several kg s^{-1} up to several tons s^{-1} (Jewitt, 2009). Dust grains emitted from Centaurs would be subject to significant perturbations by the giant planets (similar to the parent Centaurs themselves); however, short-lived, yet intense, meteoroid streams could be generated by active Centaurs at the outer planets, a topic that deserves further investigation. For our purposes here, we do not consider dust generation from Centaurs (either as meteoroid streams or as a contribution to the background dust density), as the total number of Centaurs greater than 1 km is estimated to be only ≈44,000 (Horner et al., 2004), similar to that of the EKB inner belt, which we have neglected compared to the other EKB sub-populations. Interstellar dust grains are also present throughout the Solar System, originating from near the apex of the Solar System's relative motion through the Local Interstellar Cloud (LIC) (Grün et al., 1993, 1994; Altobelli et al., 2005). These grains move along hyperbolic trajectories through the Solar System, impacting the planets are relatively large speeds (approximately 26 km/s). Despite their high speed, the mass flux of interstellar grains is several orders-of-magnitude lower than that of interplanetary grains (Grün et al., 1994), and thus, can safely be neglected in the overall calculation of dust fluxes to the outer planets.

References

A'Hearn, M.F. et al., 2005. Deep impact: Excavating Comet Tempel 1. Science 310, 258–264.

Altobelli, N. et al., 2005. Interstellar dust flux measurements by the Galileo dust instrument between the orbits of Venus and Mars. J. Geophys. Res. 110, 1–13.

Altobelli, N. et al., 2007. Cassini/Cosmic dust analyzer in situ dust measurements between Jupiter and Saturn. J. Geophys. Res. 112, 1–15.

Bézard, B. et al., 2002. Carbon monoxide on Jupiter: Evidence for both internal and external source. Icarus 159, 95–111.

Borkowski, K.J., Dwek, E., 1995. The fragmentation and vaporization of dust in grain–grain collisions. Astrophys. J. 454, 254–276.

Brownlee, D. et al., 2006. Comet 81P/Wild 2 under a microscope. Science 314, 1711–1716.

Burns, J.A., Lamy, P.L., Soter, S., 1979. Radiation forces on small particles in the Solar System. Icarus 40, 1–48.

Cassidy, T.A., Johnson, R.E., 2010. Collisional spreading of Enceladus' neutral cloud. Icarus 209, 696–703.

Cavalié, T. et al., 2010. A cometary origin for CO in the stratosphere of Saturn? Astron. Astrophys. A88, 1–7.

Cavalié, T. et al., 2014. The first submillimeter observation of CO in the stratosphere of Uranus. Astron. Astrophys. 562 A33.

Christon, S.P. et al., 2015. Discovery of suprathermal Fe^{+} in Saturn's magnetosphere. J. Geophys. Res.: Space Phys., 2720–2738.

Colwell, J.E., 1994. The disruption of planetary satellites and the creation of planetary rings. Planet. Space Sci. 42 (12), 1139–1149.

Cuzzi, J.N., Estrada, P.R., 1998. Compositional evolution of Saturn's rings due to meteoroid bombardment. Icarus 132, 1–35.

Dietzel, H. et al., 1973. The HEOS2 and Helios micrometeoroid experiments. J. Phys. E: Sci. Instrum. 6 (3), 209–217.

Dikarev, V. et al., 2005. The new ESA meteoroid model. Adv. Space Res. 25, 1282–1289.

Dikarev, V., Grün, E., 2002. New information recovered from the Pioneer 11 meteoroid experiment data. Astron. Astrophys. 383, 302–308.

Di Sisto, R.P., Fernández, J.A., Brunini, A., 2009. On the population, physical decay and orbital distribution of Jupiter family comets: Numerical simulations. Icarus 203, 140–154.

Divine, N., 1993. Five populations of interplanetary meteoroids. J. Geophys. Res. 98 (E9), 17029–17048.

Durisen, R.H. et al., 1989. Ballistic transport in planetary ring systems due to particle erosion mechanisms: I. Theory, numerical methods and illustrative examples. Icarus 80, 136–166.

Eichhorn, K., Grün, E., 1993. High-velocity impacts of dust particles in low-temperature water ice. Planet. Space Sci. 41 (6), 429–433.

Estrada, P.R. et al., 2015. Combined structural and compositional evolution of planetary rings due to micrometeoroid impacts and ballistic transport. Icarus 252, 415–439.

Feuchtgruber, H. et al., 1997. External supply of oxygen to the atmospheres of the giant planets. Nature 389, 159–162.

Feuchtgruber, H. et al., 1999. Oxygen in the stratospheres of the giant planets and Titan. In: The Universe as Seen by ISO. Paris, France, pp. 133–136.

Fleshman, B.L. et al., 2014. The roles of charge exchange and dissociation in spreading Saturn's neutral clouds. J. Geophys. Res. 117, 1–14.

Francis, P.J., 2005. The demographics of long-period comets. Astrophys. J. 635, 1348–1361.

Frisch, W., 1992. Hypervelocity impact experiments with water ice targets. Hypervel. Impacts Space, 7–14.

Fulle, M., 1992. Dust from short-period comet P/Schwassmann-Wachmann 1 and replenishment of the interplanetary dust cloud. Nature 359, 42–44.

Gladman, B. et al., 2012. The resonant trans-neptunian populations. Astron. J. 144 (23), 1–24.

Gladman, B.J., Marsden, B.G., Van Laerhoven, C., 2008. Nomenclature in the outer Solar System. In: Barucci, A., Boehnhardt, H., Cruikshank, D., Morbidelli, A. (Eds.), The Solar System Beyond Neptune, vol. 592. Univ. of Arizona Press, pp. 43–57.

Greaves, J.S. et al., 1998. A dust ring around epsilon Eridani: Analog to the young Solar System. Astrophys. J. 506, L133–L137.

Grün, E. et al., 1985. Collisional balance of the meteoric complex. Icarus 62, 244–272.

Grün, E. et al., 1993. Discovery of jovian dust streams and interstellar grains by the Ulysses spacecraft. Nature 362, 428–430.

Grün, E. et al., 1994. Interstellar dust in the heliosphere. Astron. Astrophys. 286, 915–924.

Gurnett, D.A. et al., 1997. Micron-sized dust particles detected in the outer Solar System by the Voyager 1 and 2 plasma wave instruments. Geophys. Res. Lett. 24 (24), 3125–3128.

Gustafson, B.A.S., 1994. Physics of zodiacal dust. Ann. Rev. Earth Planet. Sci. 22, 553–595.

Hahn, J.M. et al., 2002. Clementine observations of the zodiacal light and the dust content of the inner Solar System. Icarus 158, 360–378.

Han, D. et al., 2011. Constraints on dust production in the Edgeworth-Kuiper Belt from Pioneer 10 and New Horizons measurement. Geophys. Res. Lett. 38, 1–5.

Hauser, M.G. et al., 1984. IRAS observations of the diffuse infrared background. Astrophys. J. 278, L15–L18.

Hedman, M.M. et al., 2009. Three tenuous rings/arcs for three tiny moons. Icarus 199, 378–386.

Hesman, B.E. et al., 2007. The abundance profile of CO in Neptune's atmosphere. Icarus 186, 342–353.

Hillier, J.K. et al., 2007. Interplanetary dust detected by the Cassini CDA chemical analyser. Icarus 190, 643–654.

Horányi, M., 1996. Charged dust dynamics in the Solar System. Ann. Rev. Astron. Astrophys. 34, 383–418.

Horányi, M. et al., 2008. The student dust counter on the New Horizons mission. Space Sci. Rev. 140, 387–402.

Horner, J., Evans, N.W., Bailey, M.E., 2004. Simulations of the population of Centaurs – I. The bulk statistics. Mon. Not. R. Astron. Soc. 354, 798–810.

Housen, K.R., Schmidt, R.M., Holsapple, K.A., 1983. Crater ejecta scaling laws: Fundamental forms based on dimensional analysis. J. Geophys. Res.: Solid Earth 88 (B3), 2485–2499.

Humes, D.H., 1980. Results of Pioneer 10 and 11 meteoroid experiments: Interplanetary and near-Saturn. J. Geophys. Res. 85 (A11), 5841–5852.

Janches, D. et al., 2006. Modeling the global micrometeor input function in the upper atmosphere observed by high power and large aperture radars. J. Geophys. Res. 111.

Janches, D., ReVelle, D.O., 2005. Initial altitude of the micrometer phenomenon: Comparison between Arecibo radar observations and theory. J. Geophys. Res. 110, 1–19.

Jenniskens, P.M.M., 2006. Meteor Showers and their Parent Comets. Cambridge University Press.

Jenniskens, P., 2008. The IAU meteor shower nomenclature rules. Earth, Moon Planets 102 (1–4), 5–9.

Jessberger, E.K., Kissel, J., 1991. Chemical properties of cometary dust and a note on carbon isotopes. In: Newburn, Jr., R.L., Neugebauer, M., Rahe, J. (Eds.), IAU Colloq. 116: Comets in the Post-Halley Era, Astrophysics and Space Science Library, vol. 167, pp. 1075–1092.

Jewitt, D., 2009. The active Centaurs. Astron. J. 137, 4296–4312.

Jones, R.L. et al., 2006. The CFEPS Kuiper belt survey: Strategy and presurvey results. Icarus 185, 508–522.

Jurac, S., Richardson, J.D., 2007. Neutral cloud interaction with Saturn's main rings. Geophys. Res. Lett. 34, 1–7.

Kavelaars, J.J. et al., 2009. The Canada–France ecliptic plane survey – L3 data release: The orbital structure of the Kuiper Belt. Astron. J. 137, 4917–4935.

Kelley, M.S. et al., 2013. The persistent activity of Jupiter-family comets at 3–7 AU. Icarus 225, 475–494.

Kempf, S. et al., 2013. The mass flux of micrometeoroids into the saturnian system. In: AGU Fall Meeting Abstracts, vol. 1, p. 5.
Kortenkamp, S.J., Dermott, S.F., 1998. Accretion of interplanetary dust particles by the Earth. Icarus 135, 469–495.
Krivov, A.V. et al., 2002. A tenuous dust ring of Jupiter formed by escaping ejecta from the Galilean satellites. J. Geophys. Res. 107 (E1), 2-1–2-13.
Krivov, A.V. et al., 2003. Impact-generated dust clouds around planetary satellites: Spherically symmetric case. Planet. Space Sci. 51, 251–269.
Krüger, H. et al., 1999. Three years of Galileo dust data: II. 1993–1995. Planet. Space Sci. 47, 85–106.
Krüger, H. et al., 2003. Impact-generated dust clouds surrounding the Galilean moons. Icarus 164 (1), 170–187.
Krüger, H., Krivov, A.V., Grün, E., 2000. A dust cloud of Ganymede maintained by hypervelocity impacts of interplanetary micrometeoroids. Planet. Space Sci. 48 (5), 1457–1471.
Kuchner, M.J., Stark, C.C., 2010. Collisional grooming models of the Kuiper belt dust cloud. Astron. J. 140, 1007–1019.
Landgraf, M. et al., 2000. Aspects of the mass distribution of interstellar dust grains in the Solar System from in situ measurements. J. Geophys. Res. 105 (A5), 10343–10352.
Landgraf, M. et al., 2002. Origins of Solar System dust beyond Jupiter. Astron. J. 123, 2857–2861.
Lange, M.A., Ahrens, T.J., 1987. Impact experiments in low-temperature ice. Icarus 69 (3), 506–518.
Leinert, C., 1975. Zodiacal light – A measure of the interplanetary environment. Space Sci. Rev. 18, 281–339.
Lellouch, E. et al., 2002. The origin of water vapor and carbon dioxide in Jupiter's stratosphere. Icarus 159, 112–131.
Lellouch, E., Moreno, R., Paubert, G., 2005. A dual origin for Neptune's carbon monoxide? Astron. Astrophys. 430, L37–L40.
Levison, H.F. et al., 2002. The mass disruption of Oort Cloud Comets. Science 296, 2212–2215.
Levison, H.F. et al., 2006. The scattered disk as the source of Halley-type comets. Icarus 184, 619–633.
Levison, H.F., Duncan, M.J., 1997. From the Kuiper belt to Jupiter-family comets: The spatial distribution of ecliptic comets. Icarus 127, 13–32.
Liou, J.-C., Zook, H.A., 1997. Evolution of interplanetary dust particles in mean motion resonances with planets. Icarus 128 (2), 354–367.
Liou, J.-C., Zook, H.A., 1999. Signatures of the giant planets imprinted on the Edgeworth-Kuiper Belt dust disk. Astron. J. 118 (July), 580–590.
Liou, J.-C., Zook, H.A., Jackson, A.A., 1995. Radiation pressure, Poynting–Robertson drag, and solar wind drag in the restricted three-body problem. Icarus 116, 186–201.
Lisse, C.M. et al., 2006. Spitzer spectral observations of the Deep Impact ejecta. Science 313, 635–640.
Lisse, C.M. et al., 2007a. On the nature of dust in the debris disk around HD 69830. Astrophys. J. 658, 584–592.
Lisse, C.M. et al., 2007b. Comparison of the composition of the Temple 1 ejecta to the dust in Comet C/Hale-Bopp 1995 O1 and YSO HD 100546. Icarus 187, 69–86.
Lisse, C.M. et al., 2008. Circumstellar dust created by terrestrial planet formation in HD 113766. Astrophys. J. 673, 1106–1122.
Lisse, C.M. et al., 2009. Abundant circumstellar silica dust and SiO gas created by a giant hypervelocity collision in the 12 Myr HD172555 system. Astrophys. J. 701, 2019–2032.
Lisse, C.M. et al., 2012. *Spitzer* evidence for a late-heavy bombardment and the formation of ureilites in η Corvi at ~1 Gyr. Astrophys. J. 747, 1–25.
Love, S.G., Brownlee, D.E., 1993. A direct measurement of the terrestrial mass accretion rate of cosmic dust. Science 262, 550–553.
Low, F.J. et al., 1984. Infrared cirrus: New components of the extended infrared emission. Astrophys. J. 278, L19–L22.
Luszcz-Cook, S.H., de Pater, I., 2013. Constraining the origins of Neptune's carbon monoxide abundance with CARMA millimeter-wave observations. Icarus 222, 379–400.
Molina-Cuberos, J.G. et al., 2001. Ionospheric layer induced by meteoritic ionization in Titan's atmosphere. Planet. Space Sci. 49, 143–153.
Moore, L. et al., 2015. Saturn ring rain: Model estimates of water influx into Saturn's atmosphere. Icarus 245, 355–366.
Moreno, R. et al., 2012. The abundance, vertical distribution and origin of H_2O in Titan's atmosphere: Herschel observations and photochemical modelling. Icarus 221, 753–767.
Moro-Martín, A. et al., 2010. Locating planetesimal belts in the multiple-planet systems HD 128311, HD 202206, HD 82943 and HR 8799. Astrophys. J. 717, 1123–1139.
Moro-Martín, A., Malhotra, R., 2002. A study of the dynamics of dust from the Kuiper Belt: Spatial distribution and spectral energy distribution. Astron. J. 124 (October), 2305–2321.
Moro-Martín, A., Malhotra, R., 2003. Dynamical models of Kuiper Belt dust in the inner and outer Solar System. Astrophys. J. 125, 2255–2265.
Moses, J.I., 1992. Meteoroid ablation in Neptune's atmosphere. Icarus 99, 368–383.
Moses, J.I., 1997. Dust ablation during the Shoemaker-Levy 9 impacts. J. Geophys. Res. 102 (E9), 21619–21643.
Moses, J.I. et al., 2000. Photochemistry of Saturn's Atmosphere, II. Effects of an influx of external oxygen. Icarus 145, 166–202.
Moses, J.I., Bass, S.F., 2000. The effects of external material on the chemistry and structure of Saturn's ionosphere. J. Geophys. Res. 105 (E3), 7013–7052.
Nesvorný, D. et al., 2010. Cometary origin of the zodiacal cloud and carbonaceous micrometeorites: Implications for hot debris disks. Astrophys. J. 713 (April), 816–836.
Nesvorný, D. et al., 2011. Dynamics of dust particles released from Oort Cloud Comets and their contribution to radar meteors. Astrophys. J. 743 (37), 1–12.
Oort, J.H., 1950. The structure of the cloud of comets surrounding the Solar System, and a hypothesis concerning its origin. Bullet. Astron. Inst. Neth. 11 (408), 91–110.
Orton, G. et al., 1995. Collision of Comet Shoemaker-Levy 9 with Jupiter observed by the NASA infrared telescope facility. Science 267, 1277–1282.
Orton, G.S. et al., 2014. Mid-infrared spectroscopy of Uranus from the Spitzer infrared spectrometer: 2. Determination of the mean composition of the upper troposphere and stratosphere. Icarus 243, 471–493.
Petit, J. et al., 2011. The Canada–France ecliptic plane survey – Full data release: The orbital structure of the Kuiper Belt. Astron. J. 142, 1–24.
Poppe, A. et al., 2010. First results from the Venetia Burney Student Dust Counter on the New Horizons mission. Geophys. Res. Lett. 37 L11101.
Poppe, A.R., 2015. Interplanetary dust influx to the Pluto–Charon system. Icarus 246, 352–359.
Poppe, A., Horányi, M., 2011. The effect of Nix and Hydra on the putative Pluto–Charon dust cloud. Planet. Space Sci. 59, 1647–1653.
Poppe, A.R., Horányi, M., 2012. On the Edgeworth-Kuiper Belt dust flux to Saturn. Geophys. Res. Lett. 39, 1–6.
Poppe, A., James, D., Horányi, M., 2011. Measurements of the terrestrial dust influx variability by the Cosmic Dust Experiment. Planet. Space Sci. 59, 319–326.
Press, W.H. et al., 2007. Numerical Recipes: The Art of Scientific Computing, third ed. Cambridge University Press, 32 Avenue of the Americas, New York, NY 10013-2473, USA.
Sekanina, Z., 1996. Activity of Comet Hale-Bopp (1995 O1) beyond 6 AU from the Sun. Astron. Astrophys. 314, 957–965.
Spahn, F. et al., 2006. Cassini dust measurements at Enceladus and implications for the origin of the E ring. Science 311, 1416–1418.
Srama, R. et al., 2004. The Cassini cosmic dust analyzer. Space Sci. Rev. 114, 465–518.
Sremčevič, M. et al., 2005. Impact-generated dust clouds around planetary satellites: Model versus Galileo data. Planet. Space Sci. 53, 625–641.
Sremčević, M., Krivov, A.V., Spahn, F., 2003. Impact-generated dust clouds around planetary satellites: Asymmetry effects. Planet. Space Sci. 51 (June), 455–471.
Stark, C.C., Kuchner, M.J., 2008. The detectability of exo-Earths and super-Earths via resonant signatures in exozodiacal clouds. Astrophys. J. 686, 637–648.
Stark, C.C., Kuchner, M.J., 2009. A new algorithm for self-consistent three-dimensional modeling of collisions in dust debris disks. Astrophys. J. 707, 543–553.
St. Cyr, O.C. et al., 2009. STEREO SECCHI and S/WAVES observations of spacecraft debris caused by micron-size interplanetary dust impacts. Solar Phys. 256, 475–488.
Stern, S.A., 1996. Signatures of collisions in the Kuiper Disk. Astron. Astrophys. 310, 999–1010.
Stern, S.A., 2008. The New Horizons Pluto Kuiper Belt mission: An overview with historical context. Space Sci. Rev. 140, 3–21.
Szalay, J.R., Piquette, M., Horányi, M., 2013. The Student Dust Counter: Status report at 23 AU. Earth Planets Space 65, 1145–1149.
Thiessenhusen, K.-U. et al., 2002. A dust cloud around Pluto and Charon. Planet. Space Sci. 50, 79–87.
Tiscareno, M.S., Malhotra, R., 2003. The dynamics of known Centaurs. Astron. J. 126, 3122–3131.
Verbiscer, A.J., Skrutskie, M.F., Hamilton, D.P., 2009. Saturn's largest ring. Nature 461, 1098–1100.
Vitense, C., Krivov, A.V., Löhne, T., 2010. The Edgeworth-Kuiper debris disk. Astron. Astrophys. 520 (A32), 1–18.
Vitense, C., Krivov, A.V., Löhne, T., 2014. Will New Horizons see dust clumps in the Edgeworth-Kuiper Belt? Astron. J. 147, 1–8.
Volk, K., Malhotra, R., 2008. The scattered disk as the source of the Jupiter Family comets. Astrophys. J. 687, 714–725.
Wiegert, P., Tremaine, S., 1999. The evolution of long-period comets. Icarus 137, 84–121.
Wyatt, M.C. et al., 1999. How observations of circumstellar disk asymmetries can reveal hidden planets: Pericenter glow and its application to the HR 4796 disk. Astrophys. J. 527, 918–944.
Wyatt, S.P., Whipple, F.L., 1950. The Poynting–Robertson effect on meteor orbits. Astrophys. J. 111, 134–141.
Yamamoto, S., Mukai, T., 1998. Dust production by impacts of interstellar dust on Edgeworth-Kuiper Belt objects. Astron. Astrophys. 329, 785–791.
Zahnle, K., 1996. Dynamics and chemistry of SL9 plumes. In: Noll, K.S., Weaver, H.A., Feldman, P.D. (Eds.), The Collision of Comet Shoemaker-Levy 9 and Jupiter. Cambridge University Press, Cambridge, U.K, pp. 183–212.
Zahnle, K. et al., 2003. Cratering rates in the outer Solar System. Icarus 163, 263–289.
Zahnle, K., Mac Low, M., 1994. The collision of Jupiter and Comet Shoemaker-Levy 9. Icarus 108, 1–17.